

Hyperboloid GPLVM for Discovering Continuous Hierarchies via Nonparametric Estimation

Koshi Watanabe, Keisuke Maeda, Takahiro Ogawa, Miki Haseyama
Hokkaido University

Abstract

Dimensionality reduction (DR) offers a useful representation of complex high-dimensional data. Recent DR methods focus on hyperbolic geometry to derive a faithful low-dimensional representation of hierarchical data. However, existing methods are based on neighbor embedding, frequently ruining the continual relation of the hierarchies. This paper presents hyperboloid Gaussian process (GP) latent variable models (hGP-LVMs) to embed high-dimensional hierarchical data with implicit continuity via nonparametric estimation. We adopt generative modeling using the GP, which brings effective hierarchical embedding and executes ill-posed hyperparameter tuning. This paper presents three variants that employ original point, sparse point, and Bayesian estimations. We establish their learning algorithms by incorporating the Riemannian optimization and active approximation scheme of GP-LVM. For Bayesian inference, we further introduce the reparameterization trick to realize Bayesian latent variable learning. In the last part of this paper, we apply hGP-LVMs to several datasets and show their ability to represent high-dimensional hierarchies in low-dimensional spaces.

1 Introduction

With the emergence of large high-dimensional datasets, unsupervised dimensionality reduction (DR) has gained much attention in discovering a faithful low-dimensional representation holding data characteristics. Recent studies have targeted more complicated real-world

datasets than conventional toy datasets, such as neural activities (Jensen et al., 2020) or single-cell ribonucleic acid sequences (scRNA-seq) (Becht et al., 2019). They often utilize Riemannian geometry to realize effective embedding. Especially, nonlinear hierarchical relation is one of the frequently seen structures, and *hyperbolic embedding* (Nickel and Kiela, 2017, 2018), which utilizes the curved hyperbolic geometry and can perform faithful DR of hierarchies with much fewer dimensions than Euclidean cases (Sala et al., 2018). However, visualization-aided hyperbolic embedding (Klimovskaia et al., 2020; Jaquier et al., 2022) is yet to be studied extensively despite its applicability in visualizing high-dimensional hierarchical data, which is the focus of this paper.

We divide previous DRs into four classes based on two axes to clarify our standpoint: *parametric* or *nonparametric* and *data-embedding* or *neighbor-embedding*. Specifically, we consider DR with or without parametric projection between observed and latent spaces as parametric or nonparametric and DR using the data itself or neighbor relations (e.g., k -nearest neighbor graph) as data-embedding or neighbor-embedding. For example, principal component analysis (PCA) (Hotelling, 1933) and variational autoencoders (VAE) (Kingma and Welling, 2013; Higgins et al., 2017) are parametric data-embedding methods, whereas t-stochastic neighbor embedding (t-SNE) (Van der Maaten and Hinton, 2008) and uniform manifold approximation and projection (UMAP) (McInnes et al., 2018) are *nonparametric neighbor-embedding* methods. Conventionally, visualization-aided DR is realized using nonparametric neighbor-embedding methods since they do not require ill-posed parameter tuning and better preserve local structures. However, for the hierarchical data embedding, the neighbor embedding methods frequently generate clusters (Amid and Warmuth, 2019; Wang et al., 2021) and are expected to overlook the global *implicit continuity* of the hierarchical structure. This inevitable limitation of the neighbor-embedding methods motivates the introduction of *nonparametric data-embedding* approaches into visualization-aided DR for hierarchical data.

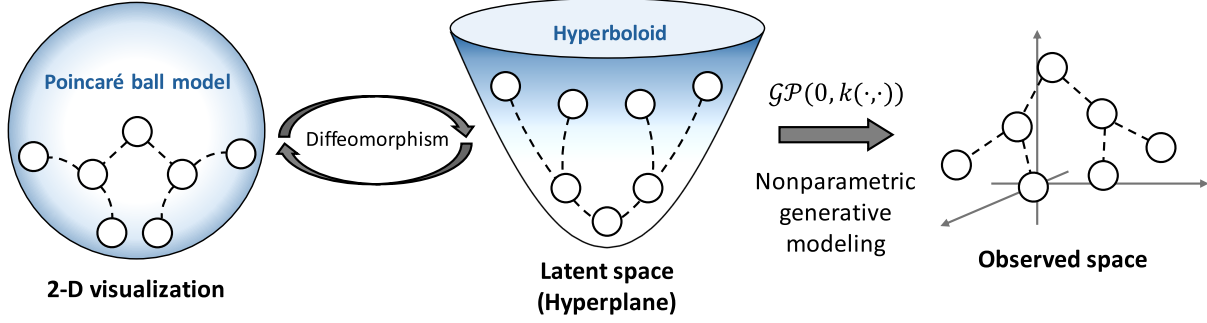


Figure 1: **An illustration of hyperboloid Gaussian process latent variable models (hGP-LVMs).** We learn the latent variables on the Lorentz model and visualize them on the Poincaré ball.

Gaussian process (GP) latent variable models (GP-LVMs) (Lawrence, 2005; Titsias and Lawrence, 2010) are one of the representatives in the nonparametric data-embedding methods. GP-LVMs assume the GP decoder of the observed variables (Rasmussen and Williams, 2006), a widely used nonparametric model for estimating unknown functions. Generative modeling between observed and latent spaces often enhances continuity and is expected to preserve the continual relation. However, recent research continues to incorporate simple Riemannian geometries in the GP (Mallasto and Feragen, 2018; Borovitskiy et al., 2020) or develop the supervised kernel methods in hyperbolic spaces (Fang et al., 2021; Fan et al., 2023), and only a few methods reach the hyperbolic extension of GP-LVM (Jaquier et al., 2022).

In this paper, we develop *hyperboloid GP-LVMs* (hGP-LVMs) to visualize the continuous hierarchies behind high-dimensional data via nonparametric estimation (Figure 1). We learn the latent variables on the Lorentz model and visualize them on the Poincaré ball by applying the diffeomorphism among them. We learn the hyperbolic latent variables by developing dedicated algorithms incorporating the previous Riemannian optimization and sparse GP methods. We formulate three variants of hGP-LVMs: the extension of the original point estimation (Lawrence, 2005), the sparse point estimation (Lawrence, 2007; Titsias, 2009), and the Bayesian estimation methods (Titsias and Lawrence, 2010; Lalchand et al., 2022) to address classical computational issues of GP and fully realize Bayesian learning of latent variables. The primary contribution of this paper is the development of novel hGP-LVMs to visualize hierarchies effectively via nonparametric estimation using generative modeling with the GP decoder. We reveal that the GP-based modeling and Bayesian estimation of the latent variables benefit the visualization-aided DR with synthetic and real-world datasets.

2 Backgrounds

We first discuss previous GP-LVMs and basic notions of the hyperbolic space for the preliminary to hGP-LVMs. Specifically, we introduce the objective functions of previous GP-LVMs and then review the hyperbolic geometry.

2.1 Gaussian Process Latent Variable Models

Let $\mathbf{y}_i \in \mathbb{R}^D$ ($i = 1, 2, \dots, N$) be D -dimensional observed variables and $\mathbf{x}_i \in \mathcal{M}^Q$ be latent variables on a Q -dimensional smooth manifold \mathcal{M}^Q . We denote $\mathbf{Y} = [\mathbf{y}_1, \mathbf{y}_2, \dots, \mathbf{y}_N]^\top \in \mathbb{R}^{N \times D}$ and $\mathbf{X} = [\mathbf{x}_1, \mathbf{x}_2, \dots, \mathbf{x}_N]^\top \in \mathbb{R}^{N \times Q}$, and let E be an Euclidean manifold. The original GP-LVM is given by

$$\mathbf{y}_{:,d} = \mathbf{f}_d(\mathbf{X}) + \boldsymbol{\epsilon}, \quad (1)$$

$$\boldsymbol{\epsilon} \sim \mathcal{N}(\mathbf{0}, \beta^{-1} \mathbf{I}_n), \quad (2)$$

$$\mathbf{f}_d \sim \mathcal{GP}(\mathbf{0}, k(\cdot, \cdot)), \quad (3)$$

where $\mathbf{f}_d \in \mathbb{R}^N$ ($d = 1, 2, \dots, D$) is a GP prior with a kernel function $k(\cdot, \cdot)$, and $\boldsymbol{\epsilon} \in \mathbb{R}^N$ is a Gaussian noise with a precision β . GP-LVM estimates the latent variables by maximizing the log-likelihood $\mathcal{F} = \sum_{d=1}^D \log p(\mathbf{y}_{:,d} | \mathbf{X})$ as follows:

$$\begin{aligned} \mathcal{F} = & -\frac{ND}{2} \log 2\pi - \frac{D}{2} \log |\mathbf{K}_{nn} + \beta^{-1} \mathbf{I}_n| \\ & - \frac{1}{2} \text{tr} \left[(\mathbf{K}_{nn} + \beta^{-1} \mathbf{I}_n)^{-1} \mathbf{Y} \mathbf{Y}^\top \right], \end{aligned} \quad (4)$$

where $\mathbf{K}_{nn} \in \mathbb{R}^{N \times N}$ is a gram matrix whose (i, j) -th entry is $k(\mathbf{x}_i, \mathbf{x}_j)$. The nonparametric estimation of latent variables is performed through the gradient-based maximization of Eq. (4). However, evaluation of Eq. (4) requires cubic time complexity $O(N^3)$, restricting the applicability of GP-LVM. Moreover, the nonlinearity of $(\mathbf{K}_{nn} + \beta^{-1} \mathbf{I}_n)^{-1}$ hinders the full Bayesian inference of \mathbf{X} . The *inducing points method* (Titsias, 2009; Bauer et al., 2016) has been used to address those issues. It assumes inducing point \mathbf{u}_d and

its positions $\mathbf{z}_k \in \mathcal{M}^Q$ ($k = 1, 2, \dots, M$) are *sufficient statistics* for the prior \mathbf{f}_d , i.e., $p(\mathbf{Y}|\mathbf{X}, \mathbf{Z}) = \prod_{d=1}^D \int p(\mathbf{y}_{:,d}|\mathbf{u}_d, \mathbf{X}, \mathbf{Z})p(\mathbf{u}_d|\mathbf{Z})d\mathbf{u}_d$, then introduces the variational inference as $\log p(\mathbf{y}_{:,d}|\mathbf{u}_d, \mathbf{X}, \mathbf{Z}) \geq \mathbb{E}_{p(\mathbf{f}_d|\mathbf{u}_d, \mathbf{X}, \mathbf{Z})} [\log p(\mathbf{y}_{:,d}|\mathbf{f}_d)]$. The objective function of the sparse GP-LVM is a tight lower bound of the log-likelihood $\sum_{d=1}^D \log p(\mathbf{y}_{:,d}|\mathbf{X}, \mathbf{Z}) \geq \hat{\mathcal{F}}$ as

$$\hat{\mathcal{F}} = -\frac{D}{2} \log \frac{(2\pi)^N |\mathbf{A}|}{\beta^N |\mathbf{K}_{mm}|} - \frac{1}{2} \text{tr}(\mathbf{W}\mathbf{Y}\mathbf{Y}^\top) - \frac{\beta D}{2} \text{tr}(\mathbf{K}_{nn}) + \frac{\beta D}{2} (\mathbf{K}_{mm}^{-1} \mathbf{K}_{mn} \mathbf{K}_{nm}), \quad (5)$$

where $\mathbf{A} = \mathbf{K}_{mm} + \beta \mathbf{K}_{mn} \mathbf{K}_{nm}$, $\mathbf{W} = \beta \mathbf{I}_n - \beta^2 \mathbf{K}_{nm} \mathbf{A}^{-1} \mathbf{K}_{mn}$, and $\mathbf{K}_{mn} = \mathbf{K}_{nm}^\top \in \mathbb{R}^{M \times N}$ are gram matrices whose (k, j) -th entry is $k(\mathbf{z}_k, \mathbf{x}_j)$. The complexity and nonlinearity problems of Eq. (4) are solved by vanishing the inversion of \mathbf{K}_{nn} . Bayesian GP-LVM estimates the approximated posterior $q(\mathbf{X}) = \prod_{i=1}^N q(\mathbf{x}_i)$ instead of the deterministic latent variables, and the objective is the evidence lower bound (ELBO) $\sum_{d=1}^D \log p(\mathbf{y}_{:,d}|\mathbf{Z}) \geq \hat{\mathcal{F}}_b$ as

$$\hat{\mathcal{F}}_b = -\frac{D}{2} \log \frac{(2\pi)^N |\mathbf{A}_b|}{\beta^N |\mathbf{K}_{mm}|} - \frac{1}{2} \text{tr}(\mathbf{W}_b \mathbf{Y} \mathbf{Y}^\top) - \frac{\beta D}{2} \text{tr}(\mathbf{K}_{nn}) + \frac{\beta D}{2} \text{tr}(\mathbf{K}_{mm}^{-1} \mathbf{\Psi}_2) - \sum_{i=1}^N \text{KL}_i, \quad (6)$$

where $\text{KL}_i = \text{KL}[q(\mathbf{x}_i)|p(\mathbf{x}_i)]$, $p(\mathbf{x}_i)$ is a prior distribution of latent variables, $\mathbf{A}_b = \mathbf{K}_{mm} + \beta \mathbf{\Psi}_2$, $\mathbf{W}_b = \beta \mathbf{I}_n - \beta^2 \mathbf{\Psi}_1^\top \mathbf{A}_b^{-1} \mathbf{\Psi}_1$, $\mathbf{\Psi}_1 = \mathbb{E}_{q(\mathbf{x})}[\mathbf{K}_{mn}]$, and $\mathbf{\Psi}_2 = \mathbb{E}_{q(\mathbf{x})}[\mathbf{K}_{mn} \mathbf{K}_{nm}]$. We give the detailed derivation from Eqns. (4) to (6) in Appendix A.1. The computational intractability of Eq. (6) frequently appears in the marginalization of $\mathbf{\Psi}$ statistics, typically solved by sampling approximation with the reparameterization trick (Salimbeni and Deisenroth, 2017; de Souza et al., 2021; Lalchand et al., 2022).

2.2 Hyperbolic Geometry

Hyperbolic spaces are smooth Riemannian manifolds and have several isometric models (Peng et al., 2021). The *Poincaré ball model* (Nickel and Kiela, 2017; Ganea et al., 2018) $\mathcal{P}^Q = (\mathbb{B}^Q, g_b)$ is a typical one in machine learning literature, where $\mathbb{B}^Q = \{\mathbf{x} \in \mathbb{R}^Q : \|\mathbf{x}\|_2 < 1\}$ and $g_b = \frac{2}{1-\|\mathbf{x}\|^2} g_e$ is the metric tensor with the Euclidean metric tensor g_e . However, the boundary $\{\mathbf{x} \in \mathbb{R}^Q : \|\mathbf{x}\|_2 = 1\}$ in the Poincaré ball model causes numerical instability. The *Lorentz model* is another one without a boundary. Formally, the Lorentz model $\mathcal{L}^Q = (\mathbb{H}^Q, g_l)$ is a Q -dimensional hyperbolic space with a Q -dimensional *upper hyperboloid* $\mathbb{H}^Q = \{\mathbf{x} = [x_0, x_1, \dots, x_Q]^\top \in \mathbb{R}^{Q+1} : \langle \mathbf{x}, \mathbf{x} \rangle_{\mathcal{L}^Q} = -1, x_0 > 0\}$ and metric tensor $g_l = \text{diag}(-1, 1, \dots, 1) \in \mathbb{R}^{(Q+1) \times (Q+1)}$, where

$\langle \mathbf{x}, \mathbf{x}' \rangle_{\mathcal{L}^Q} = -x_0 x'_0 + \sum_{i=1}^Q x_i x'_i$ is the *Lorentzian inner product*. We notice that $x_0 = \sqrt{1 + \|\tilde{\mathbf{x}}\|_2^2}$, where $\tilde{\mathbf{x}} = [x_1, x_2, \dots, x_Q]^\top$. The tangent space $\mathcal{T}_\mu \mathcal{L}^Q$ is frequently used to define functions which is the set of the tangent passes through $\mu \in \mathcal{L}^Q$. The mapping from the Lorentz model onto its tangent space at μ is explicitly stated by the exponential map $\text{Exp}_\mu(\mathbf{v}) : \mathcal{T}_\mu \mathcal{L}^Q \rightarrow \mathcal{L}^Q$ as

$$\text{Exp}_\mu(\mathbf{v}) = \cosh(\|\mathbf{v}\|_{\mathcal{L}^Q}) \mu + \sinh(\|\mathbf{v}\|_{\mathcal{L}^Q}) \frac{\mathbf{v}}{\|\mathbf{v}\|_{\mathcal{L}^Q}}, \quad (7)$$

where $\|\mathbf{v}\|_{\mathcal{L}^Q} = \sqrt{\langle \mathbf{v}, \mathbf{v} \rangle_{\mathcal{L}^Q}}$ is the norm of $\mathbf{v} \in \mathcal{T}_\mu \mathcal{L}^Q$. The length of geodesic between two points on \mathcal{L}^Q is given by

$$d_{\mathcal{L}^Q}(\mathbf{x}, \mathbf{x}') = \cosh^{-1}(-\langle \mathbf{x}, \mathbf{x}' \rangle_{\mathcal{L}^Q}). \quad (8)$$

Finally, we show the diffeomorphism $p(\mathbf{x}) : \mathcal{L}^Q \rightarrow \mathcal{P}^Q$ as

$$p(\mathbf{x}) = \frac{[x_1, x_2, \dots, x_Q]^\top}{1 + x_0}. \quad (9)$$

We learn the latent variables on the Lorentz model and visualize them on the Poincaré ball model.

3 Hyperboloid GP-LVMs

This section presents hGP-LVMs, the primary contribution of this paper. We first establish the positive definite (PD) kernel on the Lorentz model, named the *hyperboloid exponential kernel*. Next, we explain the optimization of hGP-LVMs considering the curved geometry of the latent space. For the Bayesian model in Eq. (6), straightforward optimization is not realizable due to the computational intractability included in the $\mathbf{\Psi}$ statistics and KL divergence. Thus, we develop a dedicated algorithm combining the reparameterization trick (Kingma and Welling, 2013), Riemannian optimization (Nickel and Kiela, 2018), and active set approximation in GP-LVMs (Moreno-Muñoz et al., 2022).

3.1 Hyperboloid Exponential Kernel

Although recent works use the heat kernel (Atigh et al., 2022; Niu et al., 2023; Azangulov et al., 2023) for the Riemannian kernel construction, it has a high computational cost hindering the applicability; therefore, we use the result in (Ferguson et al., 2015). It shows the following *geodesic exponential kernel*:

$$k_{\mathcal{M}}(\mathbf{x}, \mathbf{x}') = \sigma \exp\left(-\frac{d_{\mathcal{M}}(\mathbf{x}, \mathbf{x}')}{\kappa}\right), \quad (10)$$

where σ is a variance parameter and κ is a *length scale* parameter. This geodesic exponential kernel can be PD

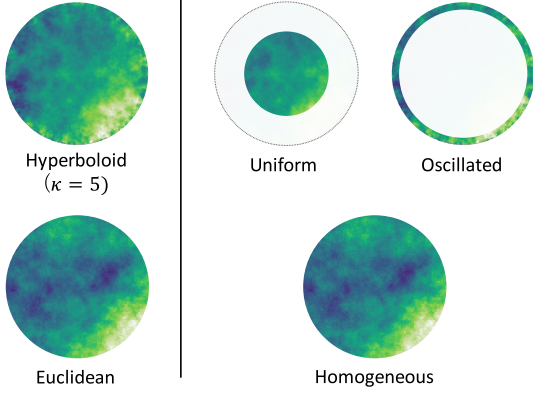


Figure 2: GP prior comparison between the hyperboloid exponential kernel (*upper*, $\kappa = 5$) and Euclidean exponential kernel (*bottom*). The color gives the value of the sampled GP. We input the latent variables on the Poincaré ball model when $\mathcal{M} = \mathcal{L}^Q$ (*left*) and those on the unit circle when $\mathcal{M} = E$ (*right*).

if $d_{\mathcal{M}}(\mathbf{x}, \mathbf{x}')$ is a conditionally negative definite (CND) metric (Feragen et al., 2015). Since the hyperbolic metric is CND (Istas, 2012), the geodesic exponential kernel in Eq. (10) when $\mathcal{M} = \mathcal{L}^Q$ is PD, and we call it the *hyperboloid exponential (HE) kernel*. Figure 2 compares the GP prior of the HE kernel and of the Euclidean exponential kernel. The prior when $\mathcal{M} = \mathcal{L}^Q$ highly correlates around the origin (similar values) and oscillates around the rim (striped values), unlike the Euclidean kernel, which is homogeneous on the entire unit circle. This heterogeneity of the hyperboloid kernel contributes to embedding the hierarchical data containing exponentially growing child nodes.

Next, we discuss the role of the HE kernel parameters σ and κ . The variance σ is similar to the general exponential kernel, determining the range of the kernel function. However, the *length scale* κ differs from that of the Euclidean kernel. The length scale of Euclidean GP-LVMs calibrates the scale of the latent variables. Although the scale in the flat Euclidean space has no structural meaning, it does not hold in the curved hyperbolic space. With a large length scale, the latent variables are widely spread on the curved manifold and strongly influenced by the hyperbolic curvature. With a small length scale, we first show one result about the relation between the distance in the Lorentz model and the Euclidean space.

Lemma 1. *Let $\mathbf{x}_1 \in \mathbb{R}^Q$ and $\mathbf{x}_2 \in \mathbb{R}^Q$ be vectors with small scales, i.e., $\|\mathbf{x}_1\|_2 \approx 0, \|\mathbf{x}_2\|_2 \approx 0$. Set $\mathbf{x}'_1 = \left[\sqrt{1 + \|\mathbf{x}_1\|_2^2}, \mathbf{x}_1^\top \right]^\top \in \mathcal{L}^Q$ and $\mathbf{x}'_2 = \left[\sqrt{1 + \|\mathbf{x}_2\|_2^2}, \mathbf{x}_2^\top \right]^\top \in \mathcal{L}^Q$, then we obtain the follow-*

Algorithm 1 Update of point latent variables.

Require: learning rate α

- 1: **while** $t < \text{max_iter}$ **do**
- 2: **for** $i = 1, 2, \dots, N$ **do**
- 3: $\mathbf{g}_i^t \leftarrow g_l^{-1} \left[\frac{\partial \mathcal{F}}{\partial x_{i0}^t}, \frac{\partial \mathcal{F}}{\partial x_{i1}^t}, \dots, \frac{\partial \mathcal{F}}{\partial x_{iQ}^t} \right]^\top$
- 4: $\mathcal{T} \mathbf{g}_i^t \leftarrow \text{proj}_{\mathbf{x}_i^t}(\mathbf{g}_i^t)$
- 5: $\mathbf{x}_i^{t+1} \leftarrow \exp_{\mathbf{x}_i^t}(-\alpha \mathcal{T} \mathbf{g}_i^t)$
- 6: **end for**
- 7: **end while**

ing result:

$$d_{\mathcal{L}^Q}(\mathbf{x}'_1, \mathbf{x}'_2) \approx d_E(\mathbf{x}_1, \mathbf{x}_2) + O(d_E(\mathbf{x}_1, \mathbf{x}_2)^3), \quad (11)$$

where $d_E(\mathbf{x}_1, \mathbf{x}_2) = \|\mathbf{x}_1 - \mathbf{x}_2\|_2$.

Proof. See Appendix A.2. □

Equation (11) indicates that the hyperboloid metric approaches the Euclidean metric around the origin asymptotically, and the HE kernel with a small length scale behaves like the Euclidean geodesic kernel. From the above, we can state that *the meaning of the length scale κ is how much we expect the latent variables to follow the hyperbolic curvature*. This metamorphosis of the length scale causes difficulty with optimization. Therefore, we treat the length scale as a predefined hyperparameter and determine it experimentally. In summary, we establish the HE kernel by extending the geodesic exponential kernel in Eq. (10) and treat the length scale as a hyperparameter to determine the degree to which latent variables follow the hyperbolic curvature.

3.2 Optimization

We apply the objective of the GP-LVM, sparse GP-LVM, and Bayesian GP-LVM with the hyperboloid kernel to learn the latent variables on the Lorentz model. The optimization challenge is the gradient computation of the latent variables, and we must consider the curved geometry of the hyperboloid. We first explain the optimization of the deterministic latent variables and extend it to the Bayesian case using *wrapped Gaussian distribution* (Nagano et al., 2019; Mathieu et al., 2019; Cho et al., 2022).

hGP-LVM and Sparse hGP-LVM. We consider the curved surfaces of the latent space by employing the Riemannian gradient descent algorithm proposed in (Nickel and Kiela, 2018). This algorithm comprises (i) computing the steepest direction, (ii) projecting the row gradients into the tangent space, and (iii) wrapping it in the surface of the Lorentz model following Eq. (7) (Algorithm 1). The row gradients

are given as $\frac{\partial \mathcal{F}}{\partial x_{iq}} = \text{tr}(\frac{\partial \mathcal{F}}{\partial \mathbf{K}} \frac{\partial \mathbf{K}}{\partial x_{iq}})$. The projection from the ambient Euclidean space to the Lorentz model $\text{proj}_{\boldsymbol{\mu}}(\mathbf{g}) : \mathbb{R}^{N+1} \rightarrow \mathcal{T}_{\boldsymbol{\mu}}\mathcal{L}^Q$ is as

$$\text{proj}_{\boldsymbol{\mu}}(\mathbf{g}) = \mathbf{g} + \langle \boldsymbol{\mu}, \mathbf{g} \rangle_{\mathcal{L}^Q} \boldsymbol{\mu}. \quad (12)$$

In the sparse hGP-LVM, the positions of the inducing points \mathbf{Z} need to be optimized in addition to the latent variables. However, their gradient-based updates cause instability in the optimization, especially in the Riemannian cases. Thus, we employ the active set approximation scheme studied in (Moreno-Muñoz et al., 2022), where we sample the inducing positions \mathbf{Z} from the latent variables \mathbf{X} at each multiple epoch.

Bayesian hGP-LVM. For probabilistic latent variable models, we first need the variational distribution $q(\mathbf{x}_i)$ and prior $p(\mathbf{x}_i)$ defined on the Lorentz models. We use the wrapped Gaussian distribution $\mathcal{N}_{\mathcal{L}^Q}^w(\mathbf{x}|\boldsymbol{\mu}, \mathbf{S})$ proposed in (Nagano et al., 2019) instead of the exact hyperbolic Gaussian for computational efficiency. We assume $q(\mathbf{x}_i) = \mathcal{N}_{\mathcal{L}^Q}^w(\mathbf{x}_i|\boldsymbol{\mu}_i, \mathbf{S}_i)$ and $p(\mathbf{x}_i) = \mathcal{N}_{\mathcal{L}^Q}^w(\mathbf{x}_i|\mathbf{0}, \mathbf{I}_q)$, where $\boldsymbol{\mu}_i \in \mathcal{L}^Q$ and $\mathbf{S}_i = \text{diag}(s_{i1}, s_{i2}, \dots, s_{iq}) \in \mathbb{R}^{Q \times Q}$ are variational parameters. The probability density function of $\mathcal{N}_{\mathcal{L}^Q}^w(\mathbf{x}_i|\boldsymbol{\mu}_i, \mathbf{S}_i)$ can be given in a closed form as

$$\mathcal{N}_{\mathcal{L}^Q}^w(\mathbf{x}|\boldsymbol{\mu}, \mathbf{S}) = \left\{ \frac{\sinh(\|\mathbf{u}\|_{\mathcal{L}^Q})}{\|\mathbf{u}\|_{\mathcal{L}^Q}} \right\}^{(Q-1)} \mathcal{N}(\mathbf{v}|\mathbf{0}, \mathbf{S}). \quad (13)$$

Since the computing of the Ψ statistics and KL divergence in Eq. (6) is no longer tractable, we approximately compute them using the sampling and the reparameterization trick. The sampling scheme of $\mathcal{N}_{\mathcal{L}^Q}^w(\mathbf{x}|\boldsymbol{\mu}, \mathbf{S})$ comprises three steps similar to the Riemannian optimization: (i) sampling $\tilde{\mathbf{v}} \sim \mathcal{N}(\mathbf{0}, \mathbf{S})$ at the origin $\boldsymbol{\mu}_0 = [1, 0, \dots, 0]^\top \in \mathcal{L}^Q$, (ii) carrying $\mathbf{v} = [0, \tilde{\mathbf{v}}^\top]^\top \in \mathcal{T}_{\boldsymbol{\mu}_0}\mathcal{L}^Q$ from the origin to an arbitrary point $\boldsymbol{\mu}$ as $\mathbf{u} = \text{PT}_{\boldsymbol{\mu}_0 \rightarrow \boldsymbol{\mu}}(\mathbf{v})$, and (iii) wrapping the vector in the surface following Eq. (7). The parallel transportation $\text{PT}_{\boldsymbol{\nu} \rightarrow \boldsymbol{\mu}}(\mathbf{v}) : \mathcal{T}_{\boldsymbol{\nu}}\mathcal{L}^Q \rightarrow \mathcal{T}_{\boldsymbol{\mu}}\mathcal{L}^Q$ is computed as follows:

$$\text{PT}_{\boldsymbol{\nu} \rightarrow \boldsymbol{\mu}}(\mathbf{v}) = \mathbf{v} + \frac{\langle \boldsymbol{\mu} - \gamma \boldsymbol{\nu}, \mathbf{v} \rangle_{\mathcal{L}^Q}}{\gamma + 1} (\boldsymbol{\mu} + \boldsymbol{\nu}), \quad (14)$$

where $\gamma = \langle \boldsymbol{\mu}, \boldsymbol{\nu} \rangle_{\mathcal{L}^Q}$. Thus, the Monte Carlo approximations of Ψ and KL divergence are given by

$$[\Psi_1]_{ik} = \sum_{h=1}^H k_{\mathcal{L}^Q}(\mathbf{x}_i^{(h)}, \mathbf{z}_k), \quad \Psi_2 = \sum_{i=1}^N \Psi_2^{(i)}, \quad (15)$$

$$[\Psi_2^{(i)}]_{kl} = \sum_{h=1}^H k_{\mathcal{L}^Q}(\mathbf{z}_k, \mathbf{x}_i^{(h)}) k_{\mathcal{L}^Q}(\mathbf{x}_i^{(h)}, \mathbf{z}_l), \quad (16)$$

$$\text{KL}_i = \sum_{h=1}^H \log \frac{\mathcal{N}_{\mathcal{L}^Q}^w(\mathbf{x}_i^{(h)}|\boldsymbol{\mu}_i, \mathbf{S}_i)}{\mathcal{N}_{\mathcal{L}^Q}^w(\mathbf{x}_i^{(h)}|\mathbf{0}, \mathbf{I}_q)}, \quad (17)$$

where H is the number of samples, and $\mathbf{x}_i^{(h)}$ is the reparameterized latent variables as

$$\mathbf{x}_i^{(h)} = \text{Exp}_{\boldsymbol{\mu}_i}(\mathbf{u}_i^{(h)}), \quad (18)$$

$$\mathbf{u}_i^{(h)} = \text{PT}_{\boldsymbol{\mu}_0 \rightarrow \boldsymbol{\mu}_i}(\mathbf{v}_i^{(h)}), \quad (19)$$

$$\tilde{\mathbf{v}}_i^{(h)} = \mathbf{S}_i^{\frac{1}{2}} \boldsymbol{\zeta}_i^{(h)}, \quad (20)$$

where $\mathbf{v}_i = [0, \tilde{\mathbf{v}}_i^{(h)\top}]^\top$ and $\boldsymbol{\zeta}_i^{(h)} \sim \mathcal{N}(\mathbf{0}, \mathbf{I}_q)$. We update the variational mean $\boldsymbol{\mu}_i$ following the Riemannian procedure in **Algorithm 1** and determine \mathbf{Z} by sampling from $\boldsymbol{\mu}_i$. The detailed computation of the row gradient $\frac{\partial \mathcal{F}_b}{\partial \boldsymbol{\mu}_i}$ and $\frac{\partial \mathcal{F}_b}{\partial \mathbf{S}_i}$ is represented in Appendix A.3.

Finally, we denote the time complexity of hGP-LVM, sparse hGP-LVM, and Bayesian hGP-LVM as $O(N^3)$, $O(M^2N + M^3)$, and $O(HM^2N + HM^3)$, respectively, which is equal to those cost of previous GP-LVM baselines.

4 Related Works

Visualization-Aided DR. t-SNE (Van der Maaten and Hinton, 2008) is the gold-standard method, and UMAP (McInnes et al., 2018) is the recent approach introducing the algebraic topology idea and realizing DR with a solid theoretical foundation. Since the neighbor embedding methods frequently overlook the global structure, the recent variants aim to catch it using a triplet loss function (Amid and Warmuth, 2019) or modifying the initial embedding (Kobak and Berens, 2019; Wang et al., 2021). DR for hierarchical data has also gained much attention, where the potential heat diffusion for affinity-based trajectory embedding (PHATE) (Moon et al., 2019) uses the diffusion operation, and PoincaréMap (Klimovskaia et al., 2020) develops the neighbor embedding on the Poincaré ball model. Visualization-aided DR methods have been widely applied in scRNA-seq analysis (Luecken and Theis, 2019), supporting the exposition of complex cell biology.

Hyperbolic Machine Learning. Previously, the hyperbolic space is used to realize the hierarchical structure learning of word taxonomies (Nickel and Kiela, 2017, 2018). Recent studies apply hyperbolic neural networks to other tasks, such as image segmentation (Atigh et al., 2022), knowledge graph embedding (Chami et al., 2020), or image-text representation learning (Desai et al., 2023). Gyrovector space equipped Möbius addition and scalar multiplication (Ganea et al., 2018) are explored to define the layer-to-layer transformation of fully connected hyperbolic networks. For unsupervised learning, VAEs with wrapped Gaussian distribution are studied extensively (Nagano et al., 2019; Mathieu et al., 2019; Cho et al., 2022). Hyperbolic kernel methods are

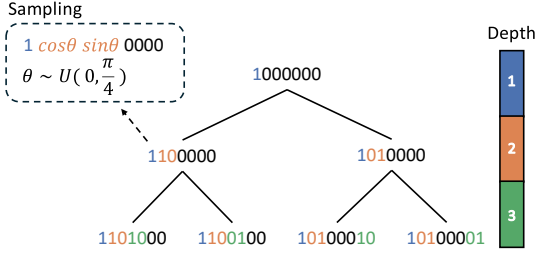


Figure 3: An illustration of the synthetic binary tree (SBT) with $d = 3$ and sampling procedure.

Table 1: Details of the SBT dataset.

	Depth		
	$d = 4$	$d = 5$	$d = 6$
# samples	300	620	1,260
# dimensions	15	31	63

also explored for support vector machines (Fan et al., 2023), and several PD kernels on the Poincaré ball are presented in (Peng et al., 2021; Yang et al., 2023).

Riemannian GP-LVM. The Matérn covariance on several curved manifolds is studied in (Borovitskiy et al., 2020), and the heat kernel in the Lie group is developed in (Azangulov et al., 2022, 2023). Only one hyperbolic extension of GP-LVMs with the hyperbolic heat kernel exists for motion taxonomy embedding in the latent space (Jaquier et al., 2022). Its objective includes sampling computation in the hyperbolic heat kernel and Ψ computation, bringing high time complexity by double sampling and is untractable for general DR with several hundreds of data points. Manifold GP-LVM (mGP-LVM) (Jensen et al., 2020) uses the geodesic exponential kernel to represent the neural curvature on simple manifolds, such as tori, Spheres, and $SO(3)$. However, manifold GP-LVM contains mathematical difficulty in the computation of the posterior distribution, which restricts the applicability of mGP-LVM to other smooth manifolds such as hyperbolic space.

5 Experiments

In this section, we show experimental results to validate our method. We first compare hGP-LVMs with Euclidean or hyperbolic generative models (Nagano et al., 2019; Cho et al., 2022). Next, we conduct visualization-aided DR with the scRNA-seq dataset and confirm the effectiveness of our methods, especially the Bayesian estimation method.

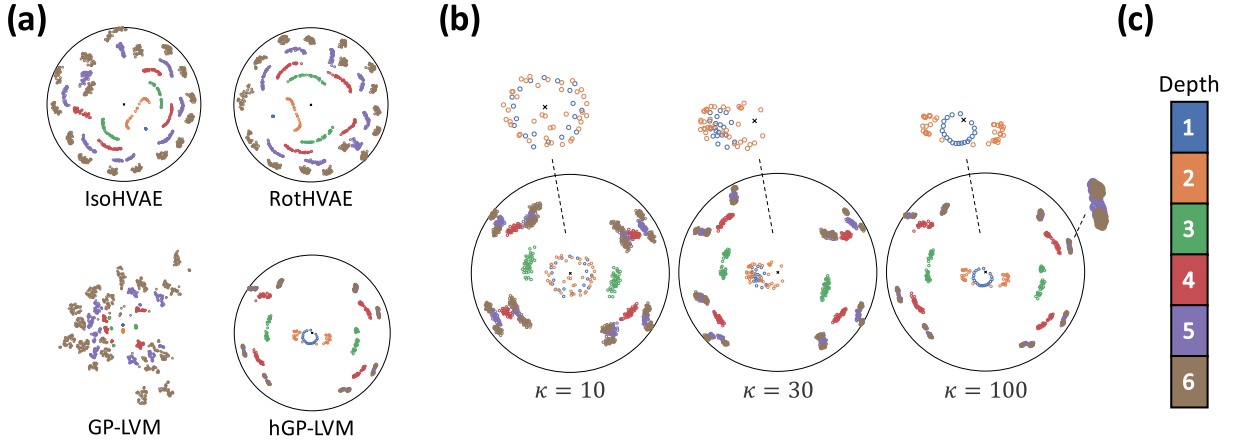
5.1 Synthetic Binary Tree Dataset

We explain the experiment on the *synthetic binary tree (SBT) dataset*, which has been used to evaluate hyperbolic generative models. This dataset is based on the SBT, exhibiting a simple hierarchical structure using binary codes. Figure 3 shows the SBT and sampling process of data points. We first determine the *depth* of the tree and then generate $(2^d - 1)$ length binary code. We get the code of each node by changing the Boolean values according to depth. By oscillating the codes, we generated datasets exhibiting tree structures of SBT. We generated 20 samples at each node with $d = 4, 5, 6$ following the previous work. The statistical details of datasets are presented in Table 1. We used the most basic hGP-LVM and set $\kappa = 100$ in all datasets. We compared hGP-LVM with GP-LVM (Lawrence, 2005), hyperbolic VAE with isotropic hyperbolic wrapped Gaussian in Eq. (13) (IsoHVAE) (Nagano et al., 2019), and Hyperbolic VAE with rotated hyperbolic wrapped Gaussian (RotHVAE) (Cho et al., 2022). We used the implementation and hyperparameter presented in (Cho et al., 2022) for hyperbolic VAEs and only searched the number of hidden units. The latent dimension of all methods was set as 2, and we compared them through quantitative evaluation and qualitative visualization. For quantitative evaluation, we used the distance correlation score between latent variables and the observed variables. The distance between latent variables was computed using the hyperbolic metric for hGP-LVM and hyperbolic VAEs and the Euclidean metric for GP-LVM. The distance between observed variables was computed with the hamming distance using the corresponding binary codes to each node.

We show the quantitative result in Table 2. We confirmed that hGP-LVM embedded the synthetic hierarchy with high-quality distance preservation than the Euclidean GP-LVM on all datasets. The priority of hGP-LVM over hyperbolic VAEs was also confirmed when $d = 5$ and $d = 6$. Although the data size was limited and more effective parameters may exist for hyperbolic VAEs, we emphasize that hGP-LVM did not require such ill-posed parameter tuning and can embed hierarchy even with a limited amount of data. We next show the visualization comparison in Figure 4 (a). In GP-LVM, it is not easy to find the hierarchical nature of the SBT dataset, and the embedding is spread with increasing depth. Although the embedding of hyperbolic VAEs represented a hierarchical nature, the root nodes with the depth 1 did not position around the origin, and it is hard to interpret the tree structure in the SBT dataset. hGP-LVM embedded the SBT’s hierarchy holding internode similarity and placed the root nodes on the origin, which largely contributed to the visibility of the embedding. In summary, we

Table 2: **Quantitative results on the SBT dataset.** We highlight the best results in blue. We computed the mean and standard deviation over 10 runs.

	Depth		
	$d = 4$	$d = 5$	$d = 6$
hGP-LVM (ours)	0.816 \pm 0.012	0.909\pm0.003	0.849\pm0.004
GP-LVM (Lawrence, 2005)	0.782 \pm 0.000	0.746 \pm 0.000	0.717 \pm 0.000
IsoHVAE (Nagano et al., 2019)	0.890 \pm 0.022	0.867 \pm 0.025	0.815 \pm 0.031
RotHVAE (Cho et al., 2022)	0.896\pm0.027	0.872 \pm 0.019	0.823 \pm 0.024


 Figure 4: **Qualitative results on the SBT dataset ($d = 6$).** (a) embedding comparison between generative models, (b) embedding of hGP-LVM with different length scales, and (c) color code of embedding.

validated the effectiveness of hGP-LVM toward generative models with the experiment typically used for evaluating hyperbolic generative models.

Embedding Comparison with Different Length-scale In Section 3.1, we state that *the meaning of the length scale κ is how much we expect the latent variables to follow the hyperbolic curvature*. We show the experimental verification of this statement in Figure 4 (b). We confirm that the representation was spread and aligned as growing κ . Although the embeddings of depths 1 and 2 were mixed around the origin when $\kappa = 10$ or $\kappa = 30$, they were separated when $\kappa = 100$. The length scale parameter determined the range of the latent variables, and large κ brought the strong hyperbolic curvature to the latent representation. We need to determine κ according to the degree to which we expected the hierarchical structure in data.

5.2 Mouse Myeloid Progenitors Dataset

We experimented with the real-world scRNA-seq dataset presented in (Paul et al., 2015). In Appendix A.5, we exhibited synthesis data results to verify the effectiveness of the GP-based approach for visualization.

This scRNA-seq dataset exhibits multiple intermediate populations of cell populations ($N = 2,730$) from the progenitors (CMP, GMP, MEP, and CLP) to the restricted myeloid cells, such as erythrocytes, leukocytes, and lymphocytes, representing the hierarchical structure along the cell differentiation. Figure 5 (a) shows the canonical hematopoietic cell lineage tree. Each cell’s features are the bag of gene expression and have labels annotated with the clusters identified in the original work. We preprocessed the original scRNA-seq data by selecting 1,000 highly-variable genes ($D = 1,000$) following (Klimovskaia et al., 2020) and (Zheng et al., 2017). The sample size is prohibitive for hGP-LVM, and we used sparse and Bayesian hGP-LVMs with $\kappa = 100$ and $M = 50$. We compared them with UMAP and PoincaréMap qualitatively and further compared with PCA (Hotelling, 1933), PHATE (Moon et al., 2019), TriMAP (Amid and Warmuth, 2019), and PacMAP (Wang et al., 2021) quantitatively. We did not take GP-LVMs since their learning was difficult under the same conditions as hGP-LVM. We used the Shepard goodness to evaluate the quality of global preservation. However, since the dataset is still noisy after preprocessing and the local structure is untrustworthy, we adopted the k -NN classification accuracy

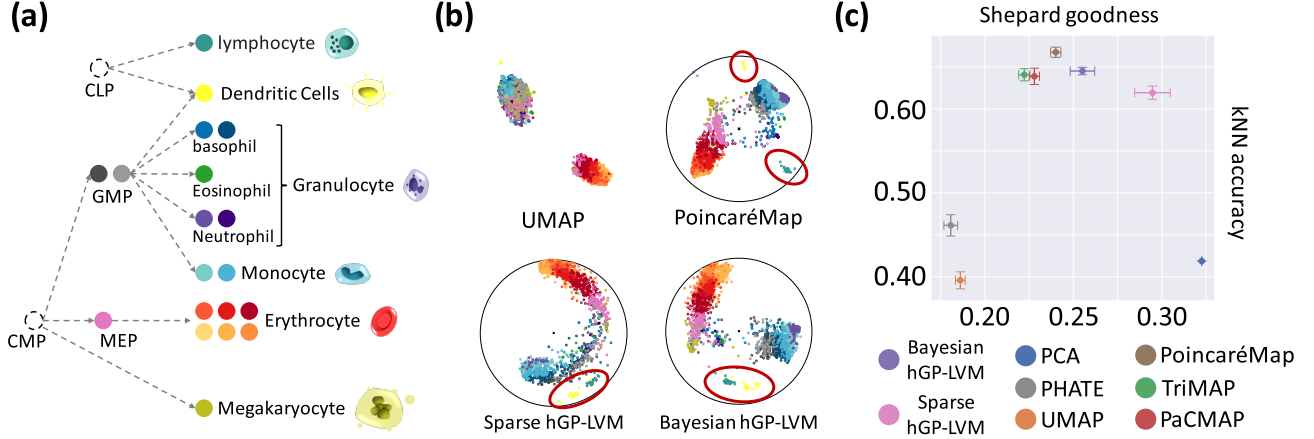


Figure 5: **Experimental results on the scRNA-seq dataset.** (a) The canonical hematopoietic cell lineage tree. (b) Two-dimensional embedding of UMAP, PoincaréMap, Sparse hGP-LVM, and Bayesian hGP-LVM. The colors correspond to those of the lineage tree. (c) The error bar plot of comparative methods. We ran the same experiment 30 times and computed the mean error with standard deviation.

($k = 5$) as the local metric to use trustworthy label information.

Figure 5 (b) shows the visualization of the scRNA-seq dataset. UMAP’s embedding was torn and mixed with the population of lymphocytes, dendritic cells, granulocytes, and monocytes. Although the PoincaréMap embedding successfully separated the cell populations, the continuity starting from MEP and GMP was not evident, and there was a large distance between the population of lymphocytes and dendritic cells that are developed from the same progenitors, CLP. The hGP-LVMs’ embedding preserved the cell population and the continuity along the development and preserved the inter-population similarity of the CLP progenitors. Furthermore, we confirmed that the megakaryocyte population of Bayesian hGP-LVM is more evident than sparse hGP-LVM. This result indicates that the uncertainty of the latent variables introduced by the full Bayesian inference is suitable for the noisy real-world dataset and brings effective embedding of the scRNA-seq dataset. Finally, we show the quantitative results in Figure 5 (c). We recall the tradeoff relationship between local and global preservation. We need both preservations to embed the hierarchical data, and hGP-LVMs show relatively high results in both metrics.

In summary, this section confirmed the effectiveness of hGP-LVMs against hyperbolic generative models and neighbor embedding methods. Although point estimation methods efficiently work for synthesizing data, Bayesian inference is needed for noisy real-world datasets. Considering the tradeoff between time complexity and representation power, we need to use them properly.

6 Conclusion

We proposed the hyperbolic extension of GP-LVMs to realize the faithful low-dimensional embedding of the hierarchical data via nonparametric estimation. We established the HE kernel and incorporated Riemannian optimization with the previous sparse GP inference method. We further introduced the reparameterization trick on the Lorentz model for a fully Bayesian estimation of the latent variables. In the experiments, we validated the embedding accuracy of hGP-LVMs with synthetic hierarchical and real-world scRNA-seq datasets and revealed the effectiveness of the GP-based modeling for visualization-aided DR.

Limitation and Future Work. We assume the hierarchical structure. If there is no clear hierarchical relation in a dataset, our method cannot embed the observed data more effectively than general GP-LVM frameworks. The computational cost might also be an issue, as it is linear to the sample size and prohibitive for several huge datasets. The embedding quality of the neighbor embedding method scales with the sample size, and they are more effective for larger datasets.

Future studies will focus on improving the Bayesian extension’s time complexity and approximated inference. The initial embedding improvement is also important to realize more efficient learning for the GP-based latent variable models.

References

Amid, E. and Warmuth, M. K. (2019). TriMap: Large-scale dimensionality reduction using triplets. *arXiv*

preprint *arXiv:1910.00204*.

- Atigh, M. G., Schoep, J., Acar, E., Van Noord, N., and Mettes, P. (2022). Hyperbolic image segmentation. In *Proceedings of the IEEE/CVF conference on Computer Vision and Pattern Recognition*, pages 4453–4462.
- Azangulov, I., Smolensky, A., Terenin, A., and Borovitskiy, V. (2022). Stationary kernels and Gaussian processes on Lie groups and their homogeneous spaces i: the compact case. *arXiv preprint arXiv:2208.14960*.
- Azangulov, I., Smolensky, A., Terenin, A., and Borovitskiy, V. (2023). Stationary kernels and Gaussian processes on Lie groups and their homogeneous spaces ii: non-compact symmetric spaces. *arXiv preprint arXiv:2301.13088*.
- Bauer, M., Van der Wilk, M., and Rasmussen, C. E. (2016). Understanding probabilistic sparse Gaussian process approximations. *Advances in Neural Information Processing Systems*, 29:1–9.
- Becht, E., McInnes, L., Healy, J., Dutertre, C.-A., Kwok, I. W., Ng, L. G., Ginhoux, F., and Newell, E. W. (2019). Dimensionality reduction for visualizing single-cell data using UMAP. *Nature Biotechnology*, 37(1):38–44.
- Borovitskiy, V., Terenin, A., Mostowsky, P., et al. (2020). Matérn Gaussian processes on Riemannian manifolds. *Advances in Neural Information Processing Systems*, 33:12426–12437.
- Chami, I., Wolf, A., Juan, D.-C., Sala, F., Ravi, S., and Ré, C. (2020). Low-dimensional hyperbolic knowledge graph embeddings. *arXiv preprint arXiv:2005.00545*.
- Cho, S., Lee, J., Park, J., and Kim, D. (2022). A rotated hyperbolic wrapped normal distribution for hierarchical representation learning. *Advances in Neural Information Processing Systems*, 35:17831–17843.
- de Souza, D., Mesquita, D., Gomes, J. P., and Matos, C. L. (2021). Learning GPLVM with arbitrary kernels using the unscented transformation. In *Proceedings of the International Conference on Artificial Intelligence and Statistics*, pages 451–459.
- Desai, K., Nickel, M., Rajpurohit, T., Johnson, J., and Vedantam, S. R. (2023). Hyperbolic image-text representations. In *Proceedings of the International Conference on Machine Learning*, pages 7694–7731.
- Fan, X., Yang, C.-H., and Vemuri, B. (2023). Horospherical decision boundaries for large margin classification in hyperbolic space. *Advances in Neural Information Processing Systems*, 36:1–11.
- Fang, P., Harandi, M., and Petersson, L. (2021). Kernel methods in hyperbolic spaces. In *Proceedings of the IEEE/CVF International Conference on Computer Vision*, pages 10665–10674.
- Feragen, A., Lauze, F., and Hauberg, S. (2015). Geodesic exponential kernels: When curvature and linearity conflict. In *Proceedings of the IEEE Conference on Computer Vision and Pattern Recognition*, pages 3032–3042.
- Ganea, O., Bécigneul, G., and Hofmann, T. (2018). Hyperbolic neural networks. *Advances in Neural Information Processing Systems*, 31:1–11.
- Higgins, I., Matthey, L., Pal, A., Burgess, C., Glorot, X., Botvinick, M., Mohamed, S., and Lerchner, A. (2017). beta-VAE: Learning basic visual concepts with a constrained variational framework. In *Proceedings of the International Conference on Learning Representations*, pages 1–22.
- Hotelling, H. (1933). Analysis of a complex of statistical variables into principal components. *Journal of Educational Psychology*, 24(6):417–441.
- Istas, J. (2012). Manifold indexed fractional fields*. *ESAIM: Probability and Statistics*, 16:222–276.
- Jaquier, N., Rozo, L., González-Duque, M., Borovitskiy, V., and Asfour, T. (2022). Bringing robotics taxonomies to continuous domains via GPLVM on hyperbolic manifolds. *arXiv preprint arXiv:2210.01672*.
- Jensen, K., Kao, T.-C., Tripodi, M., and Hennequin, G. (2020). Manifold GPLVMs for discovering non-Euclidean latent structure in neural data. *Advances in Neural Information Processing Systems*, 33:22580–22592.
- Kingma, D. P. and Welling, M. (2013). Auto-encoding variational Bayes. *arXiv preprint arXiv:1312.6114*.
- Klimovskaia, A., Lopez-Paz, D., Bottou, L., and Nickel, M. (2020). Poincaré maps for analyzing complex hierarchies in single-cell data. *Nature Communications*, 11(1):2966.
- Kobak, D. and Berens, P. (2019). The art of using t-SNE for single-cell transcriptomics. *Nature Communications*, 10(1):5416.
- Lalchand, V., Ravuri, A., and Lawrence, N. D. (2022). Generalised GPLVM with stochastic variational inference. In *Proceedings of the International Conference on Artificial Intelligence and Statistics*, pages 7841–7864.
- Lawrence, N. (2005). Probabilistic non-linear principal component analysis with Gaussian process latent variable models. *Journal of Machine Learning Research*, 6(11):1–34.
- Lawrence, N. D. (2007). Learning for larger datasets with the Gaussian process latent variable model. In *Proceedings of the International Conference on Artificial Intelligence and Statistics*, pages 243–250.

- Luecken, M. D. and Theis, F. J. (2019). Current best practices in single-cell RNA-seq analysis: a tutorial. *Molecular Systems Biology*, 15(6):e8746.
- Mallasto, A. and Feragen, A. (2018). Wrapped Gaussian process regression on Riemannian manifolds. In *Proceedings of the IEEE Conference on Computer Vision and Pattern Recognition*, pages 5580–5588.
- Mathieu, E., Le Lan, C., Maddison, C. J., Tomioka, R., and Teh, Y. W. (2019). Continuous hierarchical representations with Poincaré variational auto-encoders. *Advances in Neural Information Processing Systems*, 32:1–12.
- McInnes, L., Healy, J., and Melville, J. (2018). UMAP: Uniform manifold approximation and projection for dimension reduction. *arXiv preprint arXiv:1802.03426*.
- Moon, K. R., Van Dijk, D., Wang, Z., Gigante, S., Burkhardt, D. B., Chen, W. S., Yim, K., Elzen, A. v. d., Hirn, M. J., Coifman, R. R., et al. (2019). Visualizing structure and transitions in high-dimensional biological data. *Nature Biotechnology*, 37(12):1482–1492.
- Moreno-Muñoz, P., Feldager, C., and Hauberg, S. (2022). Revisiting active sets for Gaussian process decoders. *Advances in Neural Information Processing Systems*, 35:6603–6614.
- Nagano, Y., Yamaguchi, S., Fujita, Y., and Koyama, M. (2019). A wrapped normal distribution on hyperbolic space for gradient-based learning. In *Proceedings of the International Conference on Machine Learning*, pages 4693–4702.
- Nickel, M. and Kiela, D. (2017). Poincaré embeddings for learning hierarchical representations. *Advances in Neural Information Processing Systems*, 30:1–10.
- Nickel, M. and Kiela, D. (2018). Learning continuous hierarchies in the Lorentz model of hyperbolic geometry. In *Proceedings of the International Conference on Machine Learning*, pages 3779–3788.
- Niu, M., Dai, Z., Cheung, P., and Wang, Y. (2023). Intrinsic Gaussian process on unknown manifolds with probabilistic metrics. *Journal of Machine Learning Research*, 24(104):1–42.
- Paul, F., Arkin, Y., Giladi, A., Jaitin, D. A., Kenigsberg, E., Keren-Shaul, H., Winter, D., Lara-Astiaso, D., Gury, M., Weiner, A., et al. (2015). Transcriptional heterogeneity and lineage commitment in myeloid progenitors. *Cell*, 163(7):1663–1677.
- Peng, W., Varanka, T., Mostafa, A., Shi, H., and Zhao, G. (2021). Hyperbolic deep neural networks: A survey. *IEEE Transactions on Pattern Analysis and Machine Intelligence*, 44(12):10023–10044.
- Rasmussen, C. E. and Williams, C. K. (2006). *Gaussian Processes for Machine Learning*. MIT Press.
- Sala, F., De Sa, C., Gu, A., and Ré, C. (2018). Representation tradeoffs for hyperbolic embeddings. In *Proceedings of the International Conference on Machine Learning*, pages 4460–4469.
- Salimbeni, H. and Deisenroth, M. (2017). Doubly stochastic variational inference for deep Gaussian processes. *Advances in Neural Information Processing Systems*, 30:1–12.
- Titsias, M. (2009). Variational learning of inducing variables in sparse Gaussian processes. In *Proceedings of the International Conference on Artificial Intelligence and Statistics*, pages 567–574.
- Titsias, M. and Lawrence, N. D. (2010). Bayesian Gaussian process latent variable model. In *Proceedings of the International Conference on Artificial Intelligence and Statistics*, pages 844–851.
- Van der Maaten, L. and Hinton, G. (2008). Visualizing data using t-SNE. *Journal of Machine Learning Research*, 9(11):1–25.
- Wang, Y., Huang, H., Rudin, C., and Shaposhnik, Y. (2021). Understanding how dimension reduction tools work: an empirical approach to deciphering t-SNE, UMAP, TriMAP, and PaCMAP for data visualization. *Journal of Machine Learning Research*, 22(201):1–73.
- Yang, M., Fang, P., and Xue, H. (2023). Expanding the hyperbolic kernels: a curvature-aware isometric embedding view. In *Proceedings of the International Joint Conference on Artificial Intelligence*, pages 4469–4477.
- Zheng, G. X., Terry, J. M., Belgrader, P., Ryvkin, P., Bent, Z. W., Wilson, R., Ziraldo, S. B., Wheeler, T. D., McDermott, G. P., Zhu, J., et al. (2017). Massively parallel digital transcriptional profiling of single cells. *Nature Communications*, 8(1):14049.

Hyperboloid GPLVM for Discovering Continuous Hierarchies via Nonparametric Estimation: Supplementary Materials

A.1 Derivation of Objectives of GP-LVMs

We first recall the GP-LVM model definition as

$$\mathbf{y}_{:,d} = \mathbf{f}_d(\mathbf{X}) + \boldsymbol{\epsilon}, \quad \boldsymbol{\epsilon} \sim \mathcal{N}(\mathbf{0}, \beta^{-1} \mathbf{I}_n), \quad \mathbf{f}_d \sim \mathcal{GP}(\mathbf{0}, k(\cdot, \cdot)). \quad (\text{A.1})$$

The equal expression of Eq. (A.1) as the probabilistic density function is given by

$$\begin{aligned} p(\mathbf{y}_{:,d} | \mathbf{f}_d) &= \mathcal{N}(\mathbf{y}_{:,d} | \mathbf{f}_d, \beta^{-1} \mathbf{I}_n), \\ p(\mathbf{f}_d | \mathbf{X}) &= \mathcal{N}(\mathbf{f}_d | \mathbf{0}, \mathbf{K}_{nn}). \end{aligned}$$

Then, we derive the objective log-likelihood function of GP-LVM by marginalizing the GP prior \mathbf{f}_d as follows:

$$\begin{aligned} p(\mathbf{Y} | \mathbf{X}) &= \prod_{d=1}^D \int p(\mathbf{y}_{:,d} | \mathbf{f}_d) p(\mathbf{f}_d | \mathbf{X}) d\mathbf{f}_d \\ &= -\frac{ND}{2} \log 2\pi - \frac{D}{2} \log |\mathbf{K}_{nn} + \beta^{-1} \mathbf{I}_n| - \frac{1}{2} \text{tr} \left[(\mathbf{K}_{nn} + \beta^{-1} \mathbf{I}_n)^{-1} \mathbf{Y} \mathbf{Y}^\top \right]. \end{aligned} \quad (\text{A.2})$$

The practical problems of the GP-LVM objective in Eq. (A.2) are the computation of the $N \times N$ matrix inversion of $(\mathbf{K}_{nn} + \beta^{-1} \mathbf{I}_n)$ and log-determinant $\log |\mathbf{K}_{nn} + \beta^{-1} \mathbf{I}_n|$, which are compressed into the Cholesky decomposition of $(\mathbf{K}_{nn} + \beta^{-1} \mathbf{I}_n)$ with $O(\frac{1}{3}N^3)$ time complexity.

Next, we adopt the inducing method to derive the sparse GP-LVM objective. Formally, we assume the inducing points \mathbf{u}_d , which are sufficient statistics of the prior \mathbf{f}_d . Therefore, the joint distribution omitted \mathbf{X} and \mathbf{Z} are given by

$$p(\mathbf{y}_{:,d}, \mathbf{f}_d, \mathbf{u}_d) = p(\mathbf{y}_{:,d} | \mathbf{f}_d, \mathbf{u}_d) p(\mathbf{f}_d | \mathbf{u}_d) p(\mathbf{u}_d) \approx p(\mathbf{y}_{:,d} | \mathbf{u}_d) p(\mathbf{f}_d | \mathbf{u}_d) p(\mathbf{u}_d).$$

The marginal log-likelihood of the sparse GP model is given by

$$p(\mathbf{Y} | \mathbf{X}, \mathbf{Z}) = \prod_{d=1}^D \int p(\mathbf{y}_{:,d} | \mathbf{u}_d, \mathbf{X}, \mathbf{Z}) p(\mathbf{u}_d | \mathbf{Z}) d\mathbf{u}_d, \quad (\text{A.3})$$

where

$$\begin{aligned} p(\mathbf{y}_{:,d} | \mathbf{f}_d) &= \mathcal{N}(\mathbf{y}_{:,d} | \mathbf{f}_d, \beta^{-1} \mathbf{I}_n), \\ p(\mathbf{f}_d | \mathbf{u}_d, \mathbf{X}, \mathbf{Z}) &= \mathcal{N}(\mathbf{f}_d | \mathbf{K}_{nm} \mathbf{K}_{mm}^{-1} \mathbf{u}_d, \mathbf{K}_{nn} - \mathbf{K}_{nm} \mathbf{K}_{mm}^{-1} \mathbf{K}_{mn}), \\ p(\mathbf{y}_{:,d} | \mathbf{u}_d, \mathbf{X}, \mathbf{Z}) &= \mathcal{N}(\mathbf{y}_{:,d} | \mathbf{K}_{nm} \mathbf{K}_{mm}^{-1} \mathbf{u}_d, \mathbf{K}_{nn} - \mathbf{K}_{nm} \mathbf{K}_{mm}^{-1} \mathbf{K}_{mn} + \beta^{-1} \mathbf{I}_n), \\ p(\mathbf{u}_d | \mathbf{Z}) &= \mathcal{N}(\mathbf{f}_d | \mathbf{0}, \mathbf{K}_{mm}). \end{aligned}$$

Then, we apply the variational method with Jensen's inequality and evaluate the lower bound of the log-likelihood function as

$$\begin{aligned} \log p(\mathbf{y}_{:,d} | \mathbf{u}_d, \mathbf{X}, \mathbf{Z}) &\geq \mathbb{E}_{p(\mathbf{f}_d | \mathbf{u}_d, \mathbf{X}, \mathbf{Z})} [\log p(\mathbf{y}_{:,d} | \mathbf{f}_d)] \\ &\triangleq \mathcal{F}_1. \end{aligned}$$

Thus, we obtain the following lower bound of the log-likelihood as

$$\begin{aligned}
 \log p(\mathbf{Y}|\mathbf{X}, \mathbf{Z}) &= \log \prod_{d=1}^D \int \exp [\log p(\mathbf{y}_{:,d}|\mathbf{u}_d, \mathbf{X}, \mathbf{Z})] p(\mathbf{u}_{:,d}|\mathbf{Z}) d\mathbf{u}_d \\
 &\geq \sum_{d=1}^D \log \mathcal{N}(\mathbf{y}_{:,d}|\mathbf{0}, \mathbf{K}_{nm}\mathbf{K}_{mm}^{-1}\mathbf{K}_{mn} + \beta^{-1}\mathbf{I}_n) - \frac{D}{2} \text{tr}(\mathbf{K}_{nn} - \mathbf{K}_{nm}\mathbf{K}_{mm}^{-1}\mathbf{K}_{mn}) \\
 &= -\frac{D}{2} \log |\mathbf{Q}_{nn} + \beta^{-1}\mathbf{I}_n| - \frac{1}{2} \text{tr}[(\mathbf{Q}_{nn} + \beta^{-1}\mathbf{I}_n)^{-1}\mathbf{Y}\mathbf{Y}^\top] - \frac{\beta D}{2} \text{tr}(\mathbf{K}_{nn} - \mathbf{Q}_{nn}), \quad (\text{A.4})
 \end{aligned}$$

where $\mathbf{Q}_{nn} = \mathbf{K}_{nm}\mathbf{K}_{mm}^{-1}\mathbf{K}_{mn}$. Here, we extend Eq. (A.4) by applying the matrix determinant and inversion lemmas as

$$|\mathbf{K}_{nm}\mathbf{K}_{mm}^{-1}\mathbf{K}_{mn} + \beta^{-1}\mathbf{I}_n| = |\mathbf{K}_{mm}| |\mathbf{K}_{mm} + \beta\mathbf{K}_{mn}\mathbf{K}_{nm}|, \quad (\text{A.5})$$

$$(\mathbf{K}_{nm}\mathbf{K}_{mm}^{-1}\mathbf{K}_{mn} + \beta^{-1}\mathbf{I}_n)^{-1} = \beta\mathbf{I}_n - \beta^2\mathbf{K}_{nm}(\mathbf{K}_{mm} + \beta\mathbf{K}_{mn}\mathbf{K}_{nm})^{-1}\mathbf{K}_{mn}. \quad (\text{A.6})$$

Then, we can obtain the sparse GP-LVM objectives by substituting Eqns. (A.5) and (A.6) into Eq. (A.4) as

$$\mathcal{J} = -\frac{D}{2} \log \frac{(2\pi)^N |\mathbf{A}|}{\beta^N |\mathbf{K}_{mm}|} - \frac{1}{2} \text{tr}(\mathbf{W}\mathbf{Y}\mathbf{Y}^\top) - \frac{\beta D}{2} \text{tr}(\mathbf{K}_{nn}) + \frac{\beta D}{2} (\mathbf{K}_{mm}^{-1}\mathbf{K}_{mn}\mathbf{K}_{nm}),$$

where $\mathbf{W} = \beta\mathbf{I}_n - \beta^2\mathbf{K}_{nm}\mathbf{A}^{-1}\mathbf{K}_{mn}$ and $\mathbf{A} = \mathbf{K}_{mm} + \beta\mathbf{K}_{mn}\mathbf{K}_{nm}$.

Finally, we derive the Bayesian GP-LVM objective. We first derive the lower bound straightforwardly as

$$\begin{aligned}
 \log p(\mathbf{Y}|\mathbf{Z}) &= \sum_{d=1}^D \log \int \left\{ \int p(\mathbf{y}_{:,d}|\mathbf{u}_d, \mathbf{X}, \mathbf{Z}) p(\mathbf{u}_d) d\mathbf{u}_d \right\} p(\mathbf{X}) d\mathbf{X} \\
 &= \sum_{d=1}^D \log \int \int \exp \left[\log \left\{ p(\mathbf{y}_{:,d}|\mathbf{u}_d, \mathbf{X}, \mathbf{Z}) \frac{p(\mathbf{X})}{q(\mathbf{X})} \right\} \right] q(\mathbf{X}) p(\mathbf{u}_d) d\mathbf{X} d\mathbf{u}_d \\
 &\geq \sum_{d=1}^D \log \int \exp \left[\mathbb{E}_{q(\mathbf{X})} [\log p(\mathbf{y}_{:,d}|\mathbf{u}_d, \mathbf{X}, \mathbf{Z})] + \mathbb{E}_{q(\mathbf{X})} \left[\log \frac{p(\mathbf{X})}{q(\mathbf{X})} \right] \right] p(\mathbf{u}_d) d\mathbf{u}_d \\
 &= \sum_{d=1}^D \log \int \exp [\mathbb{E}_{q(\mathbf{X})} [\log p(\mathbf{y}_{:,d}|\mathbf{u}_d, \mathbf{X}, \mathbf{Z})]] p(\mathbf{u}_d) d\mathbf{u}_d - \text{KL}[q(\mathbf{X})||p(\mathbf{X})] \\
 &\geq \sum_{d=1}^D \log \int \exp [\mathbb{E}_{q(\mathbf{X})} [\mathcal{F}_1]] p(\mathbf{u}_d) d\mathbf{u}_d - \text{KL}[q(\mathbf{X})||p(\mathbf{X})]. \quad (\text{A.7})
 \end{aligned}$$

The expectation of \mathcal{F}_1 in Eq. (A.7) can be computed in the closed form as

$$\begin{aligned}
 \mathbb{E}_{q(\mathbf{X})} [\mathcal{F}_1] &= -\frac{\beta}{2} \mathbf{y}_{:,d}^\top \mathbf{y}_{:,d} + \beta \mathbf{y}_{:,d}^\top \mathbf{\Psi}_1 \mathbf{K}_{mm}^{-1} \mathbf{u}_d - \frac{\beta}{2} \mathbf{u}_d^\top \mathbf{K}_{mm}^{-1} \mathbf{\Psi}_2 \mathbf{K}_{mm}^{-1} \mathbf{u}_d \\
 &\quad - \frac{\beta}{2} \psi_0 + \frac{\beta}{2} \text{tr}(\mathbf{K}_{mm}^{-1} \mathbf{\Psi}_2) - \frac{N}{2} \log 2\pi\beta^{-1}. \quad (\text{A.8})
 \end{aligned}$$

By substituting Eq. (A.8) into the first term of Eq. (A.7), we obtain the following equation:

$$\begin{aligned}
 &\sum_{d=1}^D \log \int \exp [\mathbb{E}_{q(\mathbf{X})} [\mathcal{F}_1]] p(\mathbf{u}_d) d\mathbf{u}_d \\
 &= \sum_{d=1}^D \log \left[\frac{\sqrt{\beta^N |\mathbf{K}_{MM}|}}{\sqrt{(2\pi)^N |\beta \mathbf{\Psi}_2 + \mathbf{K}_{MM}|}} \exp \left\{ -\frac{1}{2} \mathbf{y}_{:,d}^\top \mathbf{W}_b \mathbf{y}_{:,d} - \frac{\beta}{2} \psi_0 + \frac{\beta}{2} \text{tr}(\mathbf{K}_{mm}^{-1} \mathbf{\Psi}_2) \right\} \right], \quad (\text{A.9})
 \end{aligned}$$

where $\psi_0 = \text{tr}[\mathbf{K}_{nn}]$, $\mathbf{W}_b = \beta\mathbf{I}_n - \beta^2\mathbf{\Psi}_1^\top \mathbf{A}_b \mathbf{\Psi}_1$ and $\mathbf{A}_b^{-1} = \mathbf{K}_{mm} + \beta\mathbf{\Psi}_2$. Finally, we expand Eq. (A.7) as

$$\mathcal{J}_b = -\frac{D}{2} \log \frac{(2\pi)^N |\mathbf{A}_b|}{\beta^N |\mathbf{K}_{mm}|} - \frac{1}{2} \text{tr}(\mathbf{W}_b \mathbf{Y}\mathbf{Y}^\top) - \frac{\beta D}{2} \psi_0 + \frac{\beta D}{2} \text{tr}(\mathbf{K}_{mm}^{-1} \mathbf{\Psi}_2) - \sum_{i=1}^N \text{KL}_i. \quad (\text{A.10})$$

A.2 Proof of Lemma 1

Recall that the Lemma is $d_{\mathcal{L}^Q}(\mathbf{x}'_1, \mathbf{x}'_2) \approx d_E(\mathbf{x}_1, \mathbf{x}_2) + O(d_E(\mathbf{x}_1, \mathbf{x}_2)^3)$ if $\|\mathbf{x}_1\|_2 \approx 0$ and $\|\mathbf{x}_2\|_2 \approx 0$.

Proof. We use the following expansion:

$$\begin{aligned}\sqrt{1+z} &= 1 + \frac{1}{2}z - \frac{1}{8}z^2 + \dots, \\ \cosh^{-1}(z) &= \sqrt{2(z-1)} \left\{ 1 - \frac{1}{12}(z-1) + \frac{3}{160}(z-1)^2 + \dots \right\}.\end{aligned}$$

The first equation is the Taylor expansion of $\sqrt{1+z}$ around $z=0$, and the second equation is derived from the Puiseux expansion of $\frac{\cosh^{-1}(z)}{\sqrt{2(z-1)}}$ around $z=1$ (Sloane, 2007). We first expand the Lorentzian inner product by substituting the Taylor expansion as

$$\begin{aligned}-\langle \mathbf{x}_1, \mathbf{x}_2 \rangle_{\mathcal{L}^Q} &= \sqrt{1 + \|\mathbf{x}_1\|_2^2} \sqrt{1 + \|\mathbf{x}_2\|_2^2} - \mathbf{x}_1^\top \mathbf{x}_2 \\ &= \left(1 + \frac{1}{2}\|\mathbf{x}_1\|_2^2 - \frac{1}{8}\|\mathbf{x}_1\|_2^4 + \dots \right) \left(1 + \frac{1}{2}\|\mathbf{x}_2\|_2^2 - \frac{1}{8}\|\mathbf{x}_2\|_2^4 + \dots \right) - \mathbf{x}_1^\top \mathbf{x}_2 \\ &\approx 1 + \frac{1}{2}\|\mathbf{x}_1\|_2^2 + \frac{1}{2}\|\mathbf{x}_2\|_2^2 - \mathbf{x}_1^\top \mathbf{x}_2 \\ &= 1 + \frac{1}{2}\|\mathbf{x}_1 - \mathbf{x}_2\|_2^2 \\ &= 1 + \frac{1}{2}d_E(\mathbf{x}_1, \mathbf{x}_2)^2.\end{aligned}$$

and then we obtain

$$\begin{aligned}d_{\mathcal{L}^Q}(\mathbf{x}_1, \mathbf{x}_2) &= \cosh^{-1}(-\langle \mathbf{x}_1, \mathbf{x}_2 \rangle_{\mathcal{L}^Q}) \\ &\approx \cosh^{-1} \left(1 + \frac{1}{2}d_E(\mathbf{x}_1, \mathbf{x}_2)^2 \right) \\ &= d_E(\mathbf{x}_1, \mathbf{x}_2) \left\{ 1 - \frac{1}{24}d_E(\mathbf{x}_1, \mathbf{x}_2)^2 + \frac{3}{640}d_E(\mathbf{x}_1, \mathbf{x}_2)^4 + \dots \right\} \\ &= d_E(\mathbf{x}_1, \mathbf{x}_2) + O(d_E(\mathbf{x}_1, \mathbf{x}_2)^3).\end{aligned}$$

□

A.3 Differentiation of hGP-LVMs

We differentiate objectives to realize the gradient-based optimization. We use the chain rules similar to the previous GP-LVM and derive the differentiation w.r.t. gram matrices. Recall the objectives of GP-LVM \mathcal{F} , Sparse GP-LVM $\hat{\mathcal{F}}$, and Bayesian GP-LVM $\hat{\mathcal{F}}_b$ as

$$\begin{aligned}\mathcal{F} &= -\frac{ND}{2} \log 2\pi - \frac{D}{2} \log |\mathbf{K}_{nn} + \beta^{-1}\mathbf{I}_n| - \frac{1}{2} \text{tr} \left[(\mathbf{K}_{nn} + \beta^{-1}\mathbf{I}_n)^{-1} \mathbf{Y} \mathbf{Y}^\top \right], \\ \hat{\mathcal{F}} &= -\frac{D}{2} \log \frac{(2\pi)^N |\mathbf{A}|}{\beta^N |\mathbf{K}_{mm}|} - \frac{1}{2} \text{tr} (\mathbf{W} \mathbf{Y} \mathbf{Y}^\top) - \frac{\beta D}{2} \text{tr} (\mathbf{K}_{nn}) + \frac{\beta D}{2} (\mathbf{K}_{mm}^{-1} \mathbf{K}_{mn} \mathbf{K}_{nm}), \\ \hat{\mathcal{F}}_b &= -\frac{D}{2} \log \frac{(2\pi)^N |\mathbf{A}_b|}{\beta^N |\mathbf{K}_{mm}|} - \frac{1}{2} \text{tr} (\mathbf{W}_b \mathbf{Y} \mathbf{Y}^\top) - \frac{\beta D}{2} \text{tr} (\mathbf{K}_{nn}) + \frac{\beta D}{2} \text{tr} (\mathbf{K}_{mm}^{-1} \boldsymbol{\Psi}_2) - \sum_{i=1}^N \text{KL}_i.\end{aligned}$$

where $\mathbf{A} = \mathbf{K}_{mm} + \beta \mathbf{K}_{mn} \mathbf{K}_{nm}$, $\mathbf{W} = \beta \mathbf{I}_n - \beta^2 \mathbf{K}_{nm} \mathbf{A}^{-1} \mathbf{K}_{mn}$, $\mathbf{A}_b = \mathbf{K}_{mm} + \beta \boldsymbol{\Psi}_2$, $\mathbf{W}_b = \beta \mathbf{I}_n - \beta^2 \boldsymbol{\Psi}_1^\top \mathbf{A}_b^{-1} \boldsymbol{\Psi}_1$, $\boldsymbol{\Psi}_1 = \mathbb{E}_{q(\mathbf{x})}[\mathbf{K}_{mn}]$, $\boldsymbol{\Psi}_2 = \mathbb{E}_{q(\mathbf{x})}[\mathbf{K}_{mn} \mathbf{K}_{nm}]$, and $\text{KL}_i = \text{KL}[q(\mathbf{x}_i) \| p(\mathbf{x}_i)]$.

A.3.1 Differentiation w.r.t. Gram Matrices

GP-LVM The gram matrix in GP-LVM in Eq. (A.2) is \mathbf{K}_{nn} . The differentiation w.r.t. \mathbf{K}_{nn} is given as follows:

$$\frac{\partial \mathcal{F}}{\partial \mathbf{K}_{nn}} = -\frac{D}{2}(\mathbf{K}_{nn} + \beta^{-1}\mathbf{I}_n)^{-1} + \frac{1}{2}(\mathbf{K}_{nn} + \beta^{-1}\mathbf{I}_n)^{-1}\mathbf{Y}\mathbf{Y}^\top(\mathbf{K}_{nn} + \beta^{-1}\mathbf{I}_n)^{-1}. \quad (\text{A.11})$$

Sparse GP-LVM The gram matrices in sparse GP-LVM are \mathbf{K}_{mn} and \mathbf{K}_{mm} . The differentiation w.r.t. \mathbf{K}_{mn} and \mathbf{K}_{mm} is given as follows:

$$\frac{\partial \dot{\mathcal{F}}}{\partial \mathbf{K}_{mn}} = -\beta D \mathbf{A}^{-1} \mathbf{K}_{mn} + \beta^2 \mathbf{A}^{-1} \mathbf{K}_{mn} \mathbf{Y} \mathbf{Y}^\top - \beta^3 \mathbf{A}^{-1} \mathbf{K}_{mn} \mathbf{Y} \mathbf{Y}^\top \mathbf{K}_{nm} \mathbf{A}^{-1} \mathbf{K}_{mn} + \beta D \mathbf{K}_{mm}^{-1} \mathbf{K}_{mn}, \quad (\text{A.12})$$

$$\frac{\partial \dot{\mathcal{F}}}{\partial \mathbf{K}_{mm}} = \frac{D}{2} \mathbf{K}_{mm}^{-1} - \frac{D}{2} \mathbf{A}^{-1} - \frac{\beta^2}{2} \mathbf{A}^{-1} \mathbf{K}_{mn} \mathbf{Y} \mathbf{Y}^\top \mathbf{K}_{nm} \mathbf{A}^{-1} - \frac{\beta D}{2} \mathbf{K}_{mm}^{-1} \mathbf{K}_{mn} \mathbf{K}_{nm} \mathbf{K}_{mm}^{-1}. \quad (\text{A.13})$$

Bayesian GP-LVM The gram matrices in Bayesian GP-LVM is Ψ_1 , Ψ_2 , and \mathbf{K}_{mm} . The differentiation w.r.t. Ψ_1 , Ψ_2 , and \mathbf{K}_{mm} is given as follows:

$$\frac{\partial \dot{\mathcal{F}}_b}{\partial \Psi_1} = \beta^2 \mathbf{A}_b \Psi_1 \mathbf{Y} \mathbf{Y}^\top, \quad (\text{A.14})$$

$$\frac{\partial \dot{\mathcal{F}}_b}{\partial \Psi_2} = -\frac{\beta D}{2} \mathbf{A}_b^{-1} - \frac{\beta^3}{2} \mathbf{A}_b^{-1} \Psi_1 \mathbf{Y} \mathbf{Y}^\top \Psi_1^\top \mathbf{A}_b^{-1} + \frac{\beta D}{2} \mathbf{K}_{mm}^{-1}, \quad (\text{A.15})$$

$$\frac{\partial \dot{\mathcal{F}}_b}{\partial \mathbf{K}_{mm}} = \frac{D}{2} \mathbf{K}_{mm}^{-1} - \frac{D}{2} \mathbf{A}_b^{-1} - \frac{\beta^2}{2} \mathbf{A}_b^{-1} \Psi_1 \mathbf{Y} \mathbf{Y}^\top \Psi_1^\top \mathbf{A}_b^{-1} - \frac{\beta D}{2} \mathbf{K}_{mm}^{-1} \Psi_2 \mathbf{K}_{mm}^{-1}. \quad (\text{A.16})$$

We can compute the gradient w.r.t. kernel parameters as

$$\frac{\partial \mathcal{F}}{\partial \sigma} = \frac{1}{\sigma} \text{tr} \left(\frac{\partial \mathcal{F}}{\partial \mathbf{K}_{nn}} \right), \quad (\text{A.17})$$

$$\frac{\partial \dot{\mathcal{F}}}{\partial \sigma} = \frac{1}{\sigma} \text{tr} \left(\frac{\partial \dot{\mathcal{F}}}{\partial \mathbf{K}_{mn}} + \frac{\partial \dot{\mathcal{F}}}{\partial \mathbf{K}_{mm}} \right), \quad (\text{A.18})$$

$$\frac{\partial \dot{\mathcal{F}}_b}{\partial \sigma} = \frac{1}{\sigma} \text{tr} \left(\frac{\partial \dot{\mathcal{F}}_b}{\partial \Psi_1} + 2 \frac{\partial \dot{\mathcal{F}}_b}{\partial \Psi_2} \right). \quad (\text{A.19})$$

A.3.2 Differentiation w.r.t. Latent Variables

Next, we derive the differentiation w.r.t. latent variables. In GP-LVM and sparse GP-LVM, the differentiation can be derived by using the chain rule as

$$\frac{\partial \mathcal{F}}{\partial x_{iq}} = \text{tr} \left(\frac{\partial \mathcal{F}}{\partial \mathbf{K}_{nn}} \frac{\partial \mathbf{K}_{nn}}{\partial x_{iq}} \right), \quad \frac{\partial \dot{\mathcal{F}}}{\partial x_{iq}} = \text{tr} \left(\frac{\partial \mathcal{F}}{\partial \mathbf{K}_{mn}} \frac{\partial \mathbf{K}_{mn}}{\partial x_{iq}} \right). \quad (\text{A.20})$$

We derive the differentiation of the gram matrix w.r.t. latent variables by entry-wise computation. The differentiation of $[\mathbf{K}_{nn}]_{ij} = k(\mathbf{x}_i, \mathbf{x}_j)$ and $[\mathbf{K}_{mn}]_{kj} = k(\mathbf{z}_k, \mathbf{x}_j)$ w.r.t. latent variables is given as follows:

$$\frac{\partial k_{\mathcal{L}^Q}(\mathbf{x}_i, \mathbf{x}_j)}{\partial x_{iq}} = \frac{k_{\mathcal{L}^Q}(\mathbf{x}_i, \mathbf{x}_j)}{\kappa \sqrt{\langle \mathbf{x}_i, \mathbf{x}_j \rangle_{\mathcal{L}^Q} - 1}} \left(x_{jq} - \frac{x_{j0}}{x_{i0}} x_{iq} \right), \quad (\text{A.21})$$

$$\frac{\partial k_{\mathcal{L}^Q}(\mathbf{z}_k, \mathbf{x}_j)}{\partial x_{iq}} = \frac{k_{\mathcal{L}^Q}(\mathbf{z}_k, \mathbf{x}_j)}{\kappa \sqrt{\langle \mathbf{z}_k, \mathbf{x}_j \rangle_{\mathcal{L}^Q} - 1}} \left(x_{jq} - \frac{x_{j0}}{z_{k0}} z_{kq} \right). \quad (\text{A.22})$$

However, the differentiation of the Bayesian hGP-LVM objective is challenging due to the reparameterization as

$$\mathbf{x}_i^{(h)} = \text{Exp}_{\mu_i}(\mathbf{u}_i^{(h)}), \quad \mathbf{u}_i^{(h)} = \text{PT}_{\mu_0 \rightarrow \mu_i}(\mathbf{v}_i^{(h)}), \quad \hat{\mathbf{v}}_i^{(h)} = \mathbf{S}_i^{\frac{1}{2}} \boldsymbol{\zeta}_i^{(h)}.$$

We first differentiate \mathcal{F}_b without the KL term. In our implementation, we use $\frac{\partial \mathcal{F}_b}{\partial \Psi_1}$ and $\frac{\partial \mathcal{F}_b}{\partial \Psi_2}$ and recall Ψ statistics as

$$\begin{aligned}\Psi_1 &= \sum_{h=1}^H \Psi_1^{(h)}, \quad [\Psi_1^{(h)}]_{kj} = k(\mathbf{z}_k, \mathbf{x}_j^{(h)}), \\ \Psi_2 &= \sum_{h=1}^H \Psi_2^{(h)}, \quad \Psi_2^{(h)} = \sum_{i=1}^N \Psi_2^{(h,i)}, \quad [\Psi_2^{(h,i)}]_{kl} = k(\mathbf{z}_k, \mathbf{x}_i^{(h)})k(\mathbf{z}_l, \mathbf{x}_i^{(h)}).\end{aligned}$$

The chain rules were used to compute the differentiation w.r.t. variational parameters as

$$\frac{\partial \mathcal{F}_b}{\partial \mu_{iq}} = \sum_{h=1}^H \text{tr} \left(\frac{\partial \mathcal{F}_b}{\partial \Psi_1^{(h)}} \frac{\partial \Psi_1^{(h)}}{\partial \mu_{iq}} + \frac{\partial \mathcal{F}_b}{\partial \Psi_2^{(h)}} \frac{\partial \Psi_2^{(h)}}{\partial \mu_{iq}} \right), \quad (\text{A.23})$$

$$\frac{\partial \mathcal{F}_b}{\partial s_{iq}} = \sum_{h=1}^H \text{tr} \left(\frac{\partial \mathcal{F}_b}{\partial \Psi_1^{(h)}} \frac{\partial \Psi_1^{(h)}}{\partial s_{iq}} + \frac{\partial \mathcal{F}_b}{\partial \Psi_2^{(h)}} \frac{\partial \Psi_2^{(h)}}{\partial s_{iq}} \right). \quad (\text{A.24})$$

We chain the differentiation to the variational parameters via latent representation $\mathbf{x}_i^{(h)}$ as

$$\begin{aligned}\frac{\partial [\Psi_1^{(h)}]_{ki}}{\partial \mu_{iq}} &= \left(\frac{\partial [\Psi_1^{(h)}]_{ki}}{\partial \mathbf{x}_i^{(h)}} \right)^\top \frac{\partial \mathbf{x}_i^{(h)}}{\partial \mu_{iq}}, & \frac{\partial [\Psi_2^{(h)}]_{kl}}{\partial \mu_{iq}} &= \left(\frac{\partial [\Psi_2^{(h)}]_{kl}^{(h,i)}}{\partial \mathbf{x}_i^{(h)}} \right)^\top \frac{\partial \mathbf{x}_i^{(h)}}{\partial \mu_{iq}}, \\ \frac{\partial [\Psi_1^{(h)}]_{ki}}{\partial s_{iq}} &= \left(\frac{\partial [\Psi_1^{(h)}]_{ki}}{\partial \mathbf{x}_i^{(h)}} \right)^\top \frac{\partial \mathbf{x}_i^{(h)}}{\partial s_{iq}}, & \frac{\partial [\Psi_2^{(h)}]_{kl}}{\partial s_{iq}} &= \left(\frac{\partial [\Psi_2^{(h)}]_{kl}^{(h,i)}}{\partial \mathbf{x}_i^{(h)}} \right)^\top \frac{\partial \mathbf{x}_i^{(h)}}{\partial s_{iq}},\end{aligned}$$

where the differentiation of the gram matrices is given as

$$\frac{\partial [\Psi_1^{(h)}]_{ki}}{\partial \mathbf{x}_i^{(h)}} = \frac{k_{\mathcal{LQ}}(\mathbf{z}_k, \mathbf{x}_i^{(h)})}{\kappa \sqrt{\langle \mathbf{z}_k, \mathbf{x}_i^{(h)} \rangle_{\mathcal{LQ}} - 1}} \left(x_{iq}^{(h)} - \frac{x_{i0}^{(h)}}{z_{k0}} z_{kq} \right), \quad (\text{A.25})$$

$$\begin{aligned}\frac{\partial [\Psi_2^{(h,i)}]_{kl}}{\partial \mathbf{x}_i^{(h)}} &= \frac{k_{\mathcal{LQ}}(\mathbf{z}_k, \mathbf{x}_i^{(h)})k_{\mathcal{LQ}}(\mathbf{z}_l, \mathbf{x}_i^{(h)})}{\kappa \sqrt{\langle \mathbf{z}_k, \mathbf{x}_i^{(h)} \rangle_{\mathcal{LQ}} - 1}} \left(x_{jq}^{(h)} - \frac{x_{j0}^{(h)}}{z_{k0}} z_{kq} \right) \\ &\quad + \frac{k_{\mathcal{LQ}}(\mathbf{z}_k, \mathbf{x}_i^{(h)})k_{\mathcal{LQ}}(\mathbf{z}_l, \mathbf{x}_i^{(h)})}{\kappa \sqrt{\langle \mathbf{z}_l, \mathbf{x}_i^{(h)} \rangle_{\mathcal{LQ}} - 1}} \left(x_{jq}^{(h)} - \frac{x_{j0}^{(h)}}{z_{l0}} z_{lq} \right).\end{aligned} \quad (\text{A.26})$$

Finally, we derive the differentiation of $\mathbf{x}_i^{(h)}$ w.r.t. variational parameters by chaining the reparameterization. Let $\mathbb{1}_q \in \mathbb{R}^{Q+1}$ be a one-hot vector whose $(q+1)$ -th element is 1. We first derive w.r.t. variational mean μ_{iq} as

$$\begin{aligned}\frac{\partial \mathbf{x}_i^{(h)}}{\partial \mu_{iq}} &= \cosh(\|\mathbf{u}_i^{(h)}\|_{\mathcal{LQ}}) \mathbb{1}_q + \frac{\partial}{\partial \mu_{iq}} \left\{ \cosh(\|\mathbf{u}_i^{(h)}\|_{\mathcal{LQ}}) \right\} \boldsymbol{\mu}_i \\ &\quad + \frac{\partial}{\partial \mu_{iq}} \left\{ \frac{\sinh(\|\mathbf{u}_i^{(h)}\|_{\mathcal{LQ}})}{\|\mathbf{u}_i^{(h)}\|_{\mathcal{LQ}}} \right\} \mathbf{u}_i^{(h)} + \frac{\sinh(\|\mathbf{u}_i^{(h)}\|_{\mathcal{LQ}})}{\|\mathbf{u}_i^{(h)}\|_{\mathcal{LQ}}} \frac{\partial \mathbf{u}_i^{(h)}}{\partial \mu_{iq}}.\end{aligned} \quad (\text{A.27})$$

We then compute the differentiation of the second and third terms in Eq. (A.27) as

$$\frac{\partial}{\partial \mu_{iq}} \left\{ \cosh(\|\mathbf{u}_i^{(h)}\|_{\mathcal{LQ}}) \right\} = \frac{\sinh(\|\mathbf{u}_i^{(h)}\|_{\mathcal{LQ}})}{\|\mathbf{u}_i^{(h)}\|_{\mathcal{LQ}}} \cdot \hat{\mathbf{u}}_i^{(h)\top} \frac{\partial \mathbf{u}_i^{(h)}}{\partial \mu_{iq}}, \quad (\text{A.28})$$

$$\frac{\partial}{\partial \mu_{iq}} \left\{ \frac{\sinh(\|\mathbf{u}_i^{(h)}\|_{\mathcal{LQ}})}{\|\mathbf{u}_i^{(h)}\|_{\mathcal{LQ}}} \right\} = \frac{\cosh(\|\mathbf{u}_i^{(h)}\|_{\mathcal{LQ}}) \|\mathbf{u}_i^{(h)}\|_{\mathcal{LQ}} - \sinh(\|\mathbf{u}_i^{(h)}\|_{\mathcal{LQ}})}{\|\mathbf{u}_i^{(h)}\|_{\mathcal{LQ}}^3} \cdot \hat{\mathbf{u}}_i^{(h)\top} \frac{\partial \mathbf{u}_i^{(h)}}{\partial \mu_{iq}}, \quad (\text{A.29})$$

where $\hat{\mathbf{u}}_i = [-u_{i0}, u_{i1}, \dots, u_{iQ}]^\top$. The differentiation of $\mathbf{u}_i^{(h)}$ given as

$$\frac{\partial \mathbf{u}_i^{(h)}}{\partial \mu_{iq}} = \begin{cases} -\frac{\tilde{\boldsymbol{\mu}}_i^\top \tilde{\mathbf{v}}_i^{(h)}}{(\mu_{i0}+1)^2}(\boldsymbol{\mu}_0 + \boldsymbol{\mu}_i) + \frac{\tilde{\boldsymbol{\mu}}_i^\top \tilde{\mathbf{v}}_i^{(h)}}{\mu_{i0}+1} \mathbb{1}_0 & (q=0), \\ \frac{\tilde{v}_{iq}}{\mu_{i0}+1}(\boldsymbol{\mu}_0 + \boldsymbol{\mu}_i) + \frac{\tilde{\boldsymbol{\mu}}_i^\top \tilde{\mathbf{v}}_i^{(h)}}{\mu_{i0}+1} \mathbb{1}_q & (q \neq 0). \end{cases} \quad (\text{A.30})$$

Next, we derive the differentiation w.r.t. variational variance s_{iq} as

$$\frac{\partial \mathbf{x}_i}{\partial s_{iq}} = \frac{\partial}{\partial s_{iq}} \left\{ \cosh(\|\mathbf{u}_i^{(h)}\|_{\mathcal{L}^Q}) \right\} \boldsymbol{\mu}_i + \frac{\partial}{\partial s_{iq}} \left\{ \frac{\sinh(\|\mathbf{u}_i^{(h)}\|_{\mathcal{L}^Q})}{\|\mathbf{u}_i^{(h)}\|_{\mathcal{L}^Q}} \right\} \mathbf{u}_i^{(h)} + \frac{\sinh(\|\mathbf{u}_i^{(h)}\|_{\mathcal{L}^Q})}{\|\mathbf{u}_i^{(h)}\|_{\mathcal{L}^Q}} \frac{\partial \mathbf{u}_i^{(h)}}{\partial s_{iq}}. \quad (\text{A.31})$$

We compute the first and second terms in Eq. (A.31) as

$$\frac{\partial}{\partial s_{iq}} \left\{ \cosh(\|\mathbf{u}_i^{(h)}\|_{\mathcal{L}^Q}) \right\} = \frac{\sinh(\|\mathbf{u}_i^{(h)}\|_{\mathcal{L}^Q})}{\|\mathbf{u}_i^{(h)}\|_{\mathcal{L}^Q}} \cdot \hat{\mathbf{u}}_i^{(h)\top} \frac{\partial \mathbf{u}_i^{(h)}}{\partial s_{iq}}, \quad (\text{A.32})$$

$$\frac{\partial}{\partial s_{iq}} \left\{ \frac{\sinh(\|\mathbf{u}_i^{(h)}\|_{\mathcal{L}^Q})}{\|\mathbf{u}_i^{(h)}\|_{\mathcal{L}^Q}} \right\} = \frac{\cosh(\|\mathbf{u}_i^{(h)}\|_{\mathcal{L}^Q}) \|\mathbf{u}_i^{(h)}\|_{\mathcal{L}^Q} - \sinh(\|\mathbf{u}_i^{(h)}\|_{\mathcal{L}^Q})}{\|\mathbf{u}_i^{(h)}\|_{\mathcal{L}^Q}^3} \cdot \hat{\mathbf{u}}_i^{(h)\top} \frac{\partial \mathbf{u}_i^{(h)}}{\partial s_{iq}}. \quad (\text{A.33})$$

Then, the differentiation of \mathbf{u}_i w.r.t. s_{iq} is derived as

$$\frac{\partial \mathbf{u}_i^{(h)}}{\partial s_{iq}} = \zeta_{iq}^{(h)} \mathbb{1}_q + \frac{\mu_{iq} \zeta_{iq}^{(h)}}{\mu_{i0} + 1} (\boldsymbol{\mu}_0 + \boldsymbol{\mu}_i). \quad (\text{A.34})$$

Finally, we compute the differentiation of the KL term. We first extend the KL term with Monte Carlo approximations as

$$\begin{aligned} \text{KL}_i &= \sum_{h=1}^H \left\{ \log \mathcal{N}_{\mathcal{L}^Q}^w(\mathbf{x}_i^{(h)} | \boldsymbol{\mu}_i, \mathbf{S}_i) - \log \mathcal{N}_{\mathcal{L}^Q}^w(\mathbf{x}_i^{(h)} | \mathbf{0}, \mathbf{I}_n) \right\} \\ &= \sum_{h=1}^H \left\{ \log \mathcal{N}(\mathbf{v}_i^{(h)} | \mathbf{0}, \mathbf{S}_i) - (Q-1) \log \frac{\sinh(\|\mathbf{u}_i^{(h)}\|_{\mathcal{L}^Q})}{\|\mathbf{u}_i^{(h)}\|_{\mathcal{L}^Q}} \right. \\ &\quad \left. - \log \mathcal{N}(\mathbf{v}_i^{(h)} | \mathbf{0}, \mathbf{I}_n) + (Q-1) \log \frac{\sinh(\|\mathbf{v}_i^{(h)}\|_{\mathcal{L}^Q})}{\|\mathbf{v}_i^{(h)}\|_{\mathcal{L}^Q}} \right\}, \end{aligned} \quad (\text{A.35})$$

where

$$\begin{aligned} \log \mathcal{N}(\mathbf{v}_i^{(h)} | \mathbf{0}, \mathbf{S}_i) &= -\frac{Q}{2} \log 2\pi - \frac{1}{2} \log |\mathbf{S}_i| - \frac{1}{2} \boldsymbol{\zeta}_i^{(h)\top} \boldsymbol{\zeta}_i^{(h)}, \\ \log \mathcal{N}(\mathbf{v}_i^{(h)} | \mathbf{0}, \mathbf{I}_n) &= -\frac{Q}{2} \log 2\pi - \frac{1}{2} \boldsymbol{\zeta}_i^{(h)\top} \mathbf{S}_i \boldsymbol{\zeta}_i^{(h)}. \end{aligned}$$

Its differentiation can be computed using Eqns. (A.30) and (A.34). The differentiation of the second and fourth terms is given as

$$\begin{aligned} \frac{\partial}{\partial \mu_{iq}} \left\{ \log \frac{\sinh(\|\mathbf{u}_i^{(h)}\|_{\mathcal{L}^Q})}{\|\mathbf{u}_i^{(h)}\|_{\mathcal{L}^Q}} \right\} &= \left\{ \frac{1}{\tanh(\|\mathbf{u}_i^{(h)}\|_{\mathcal{L}^Q}) \|\mathbf{u}_i^{(h)}\|_{\mathcal{L}^Q}} - \frac{1}{\|\mathbf{u}_i^{(h)}\|_{\mathcal{L}^Q}} \right\} \cdot \hat{\mathbf{u}}_i^{(h)\top} \frac{\partial \mathbf{u}_i^{(h)}}{\partial \mu_{iq}}, \\ \frac{\partial}{\partial s_{iq}} \left\{ \log \frac{\sinh(\|\mathbf{u}_i^{(h)}\|_{\mathcal{L}^Q})}{\|\mathbf{u}_i^{(h)}\|_{\mathcal{L}^Q}} \right\} &= \left\{ \frac{1}{\tanh(\|\mathbf{u}_i^{(h)}\|_{\mathcal{L}^Q}) \|\mathbf{u}_i^{(h)}\|_{\mathcal{L}^Q}} - \frac{1}{\|\mathbf{u}_i^{(h)}\|_{\mathcal{L}^Q}} \right\} \cdot \hat{\mathbf{u}}_i^{(h)\top} \frac{\partial \mathbf{u}_i^{(h)}}{\partial s_{iq}}, \\ \frac{\partial}{\partial s_{iq}} \left\{ \log \frac{\sinh(\|\mathbf{v}_i^{(h)}\|_{\mathcal{L}^Q})}{\|\mathbf{v}_i^{(h)}\|_{\mathcal{L}^Q}} \right\} &= \left\{ \frac{1}{\tanh(\|\mathbf{u}_i^{(h)}\|_{\mathcal{L}^Q}) \|\mathbf{u}_i^{(h)}\|_{\mathcal{L}^Q}} - \frac{1}{\|\mathbf{u}_i^{(h)}\|_{\mathcal{L}^Q}} \right\} \frac{\zeta_{iq}^{(h)}}{\sqrt{s_{iq}}}. \end{aligned}$$

A.4 Experimental Details

We implemented our methods partially using the GPy (GPy, 2012) source code (BSD-3-Clause license) and experimented partially using PoincaréMap (CC BY-NC 4.0 license) (Klimovskaia et al., 2020) and RotHVAE (Cho et al., 2022), sincerely appreciating their contribution. Our code ran on a single Intel Core i7-10700 CPU without GPU. Before inference, the latent variables of hGP-LVM and sparse hGP-LVM and the variational mean of Bayesian hGP-LVM were initialized by generating two-dimensional random variables following $U(-10^{-3}, 10^{-3})$ and then mapping them into the Lorentz model as $[\sqrt{1 + x_1^2 + x_2^2}, x_1, x_2]^\top$. We initialized the variance parameter $U(-10^{-5}, 10^{-5})$ in the Bayesian hGP-LVM. During optimization, we set a large learning rate at the beginning of optimization and fixed variance parameters in the first 100 epochs for Bayesian hGP-LVM. The position of inducing variables \mathbf{Z} was updated every 10 epoch by sampling from latent variables.

We next notified the details of the quality metrics we used. Trustworthiness $T(k) \in [0, 1]$ is a local one and defined as follows:

$$T(k) = 1 - \frac{2}{Nk(2N - 3k - 1)} \sum_{i=1}^N \sum_{j \in U_i^k} \max(0, r(i, j) - k), \quad (\text{A.36})$$

where U_i^k denotes a set of the k -nearest neighbors of the sample i in the *latent* space, and j is an $r(i, j)$ -th neighbor of i . Continuity $C(k)$ is the converse of trustworthiness computed by changing U_i^k in Eq. (A.36) into V_i^k , a set of the k -nearest neighbors of the sample i in the *observed* space. The Shepard goodness is the Spearman rank correlation in the Shepard diagram. The Shepard diagram is the scatterplot of the pointwise distance between two variables, and there are $\frac{N(N-1)}{2}$ points corresponding to the distance value between any two variables. The quality metrics for DR are compared in (Espadoto et al., 2019).

A.5 Additional Experimental Results

In this section, we show the additional experimental results to compare our methods with the visualization-aided DR methods using synthesis datasets.

Spiral. First, we validate the effectiveness of the GP to preserve the continuity with the *Spiral* dataset. The Spiral dataset contains 10 spirals starting from the origin with random oscillation in proportion to the norm (Figure A.1 (a)), synthesizing easy hierarchies. We generated 10 spirals with 80 points in a two-dimensional space ($N = 800$) and mapped them in a 20-dimensional space through a random linear transformation ($D = 20$). We embedded the Spiral into the two-dimensional space and compared the quality with quantitative metrics and qualitative visualization. For quantitative evaluation, we used the three metrics following (Espadoto et al., 2019; Zu and Tao, 2022) to evaluate the preservation quality of the local and global structure: trustworthiness (Venna and Kaski, 2001), continuity, and Shepard goodness (Joia et al., 2011). Trustworthiness tells the reliability of the embedding, and continuity measures the preservation quality of the local continuity. The local metrics require the number of neighbors, and we set $k = 3$ in both metrics. The Shepard goodness is a global metric and the Spearman rank correlation of the pointwise distances between observed and latent variables. The Shepard goodness measures the match of global coordinates between variables. Since we expected the visualization purposes, we computed each metric using Euclidean coordinates. We compared hGP-LVMs with UMAP (McInnes et al., 2018) as a benchmark for DR, and PoincaréMap (Klimovskaia et al., 2020) as a DR method on the hyperbolic model to confirm the effectiveness of the GP-based modeling. We set $\kappa = 100$ and $M = 30$ in all hGP-LVMs and conducted the same experiment ten times to confirm the reproducibility.

We first show the quantitative results in Figure A.1 (b). hGP-LVM and sparse hGP-LVM performed the highest results with low variances in all metrics, indicating that they preserved Spirals' global and local structure. However, Bayesian hGP-LVM contains high variance in the local metrics caused by the approximated inference. Figure A.1 (c) shows that UMAP and PoincaréMap preferred the neighbor relations of Spiral, unlike that of hGP-LVM, which preferred their global coordinates. The results in Figures A.1 (b) and (c) imply that local and global structure preservation is needed to embed the continuity of structured data. Figure A.1 (d) shows the detailed results to confirm the effect of the length scale parameter κ . The range of the latent variables spread with large κ , and the continuity score increased, which comes in the hyperbolic curvature of the latent space. However, the Shepard goodness score decreased with large κ , and we observed the tradeoff relationship between global and

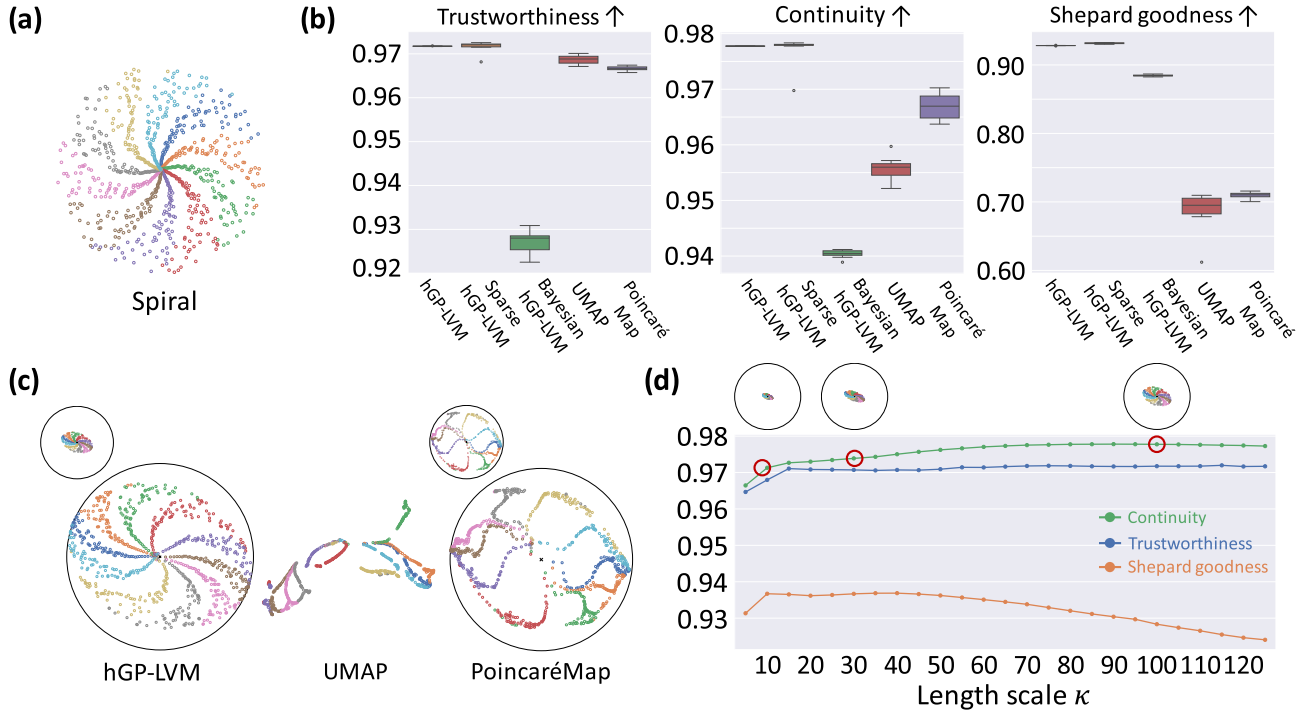


Figure A.1: **Experimental results on the Spiral dataset.** (a) Shape of the spirals before linear transformation. (b) Error bar plot of trustworthiness (left), continuity (center), and Shepard goodness (right). (c) Scatter plot of two-dimensional embeddings of hGP-LVM, UMAP, and PoincaréMap. We zoomed in on latent variables and showed the original latent space in the upper left corner. (d) Quality metric scores of hGP-LVM with different length scales κ . (e) Comparison of reconstruction error of sparse hGP-LVM and sparse GP-LVM.

local preservation quality. From the above, we confirm that hGP-LVMs have higher results than comparatives in the Spiral dataset.

Synthetic Myeloid Progenitors (Klimovskaia et al., 2020). We show another synthetic experimental results on the Myeloid Progenitors (MP) dataset, synthesizing cell differentiation from the progenitors into four cells: erythrocyte, neutrophil, monocyte, and megakaryocyte ($N = 640$, $D = 11$) (Figure A.2 (a)). We set $\kappa = 100$ and $M = 50$.

Figure A.2 (b) shows the quantitative results. hGP-LVM outperformed the comparative methods except for the local metrics. However, the absolute value was still high, and hGP-LVM produced high accuracy in both local and global metrics. Figure A.2 (c) shows the visualization results of hGP-LVM, GP-LVM, and PoincaréMap. Although the embeddings of GP-LVM and PoincaréMap are torn or wiggling, the hGP-LVM well preserved the continuity behind the hierarchical data, contributing to the visibility of the low-dimensional embeddings. The effect of the length scale in Figures A.1 (d) is similar to the result on the Spiral dataset in Figure A.2 (d). From the above, we confirm that hGP-LVMs produced better results than previous visualization-aided DR methods in the synthetic setting.

A.5.1 Embedding Comparison with Different Lengthscale

This section presents the visualization comparison with different length scales, κ . In Section 3.1 of the main paper, we state that *the meaning of the length scale κ is how much we expect the latent variables to follow the hyperbolic curvature*. We show the experimental verification of this statement in Figure A.3 on all synthesis datasets. In all results, we can confirm that the representation was spread and aligned as growing κ . In the SBT results (bottom), although the embeddings of depths 1 and 2 were mixed around the origin, they were separated with $\kappa = 100$. The length scale parameter determined the range of the latent variables, and large κ brought the hyperbolic curvature to the latent representation. We must determine κ according to the degree to which we expected the hierarchical structure in data.

References

- Cho, S., Lee, J., Park, J., and Kim, D. (2022). A rotated hyperbolic wrapped normal distribution for hierarchical representation learning. *Advances in Neural Information Processing Systems*, 35:17831–17843.
- Espadoto, M., Martins, R. M., Kerren, A., Hirata, N. S., and Telea, A. C. (2019). Toward a quantitative survey of dimension reduction techniques. *IEEE Transactions on Visualization and Computer Graphics*, 27(3):2153–2173.
- GPy (2012). GPy: A Gaussian process framework in Python. Available: <http://github.com/SheffieldML/GPy>.
- Joia, P., Coimbra, D., Cuminato, J. A., Paulovich, F. V., and Nonato, L. G. (2011). Local affine multidimensional projection. *IEEE Transactions on Visualization and Computer Graphics*, 17(12):2563–2571.
- Klimovskaia, A., Lopez-Paz, D., Bottou, L., and Nickel, M. (2020). Poincaré maps for analyzing complex hierarchies in single-cell data. *Nature Communications*, 11(1):2966.
- McInnes, L., Healy, J., and Melville, J. (2018). UMAP: Uniform manifold approximation and projection for dimension reduction. *arXiv preprint arXiv:1802.03426*.
- Sloane, N. J. (2007). The on-line encyclopedia of integer sequences. In *Proceedings of the International Conference on Towards Mechanized Mathematical Assistants*, pages 130–130.
- Venna, J. and Kaski, S. (2001). Neighborhood preservation in nonlinear projection methods: An experimental study. In *Proceedings of the International Conference on Artificial Neural Networks*, pages 485–491.
- Zu, X. and Tao, Q. (2022). SpaceMAP: Visualizing high-dimensional data by space expansion. In *Proceedings of the International Conference on Machine Learning*, pages 27707–27723.

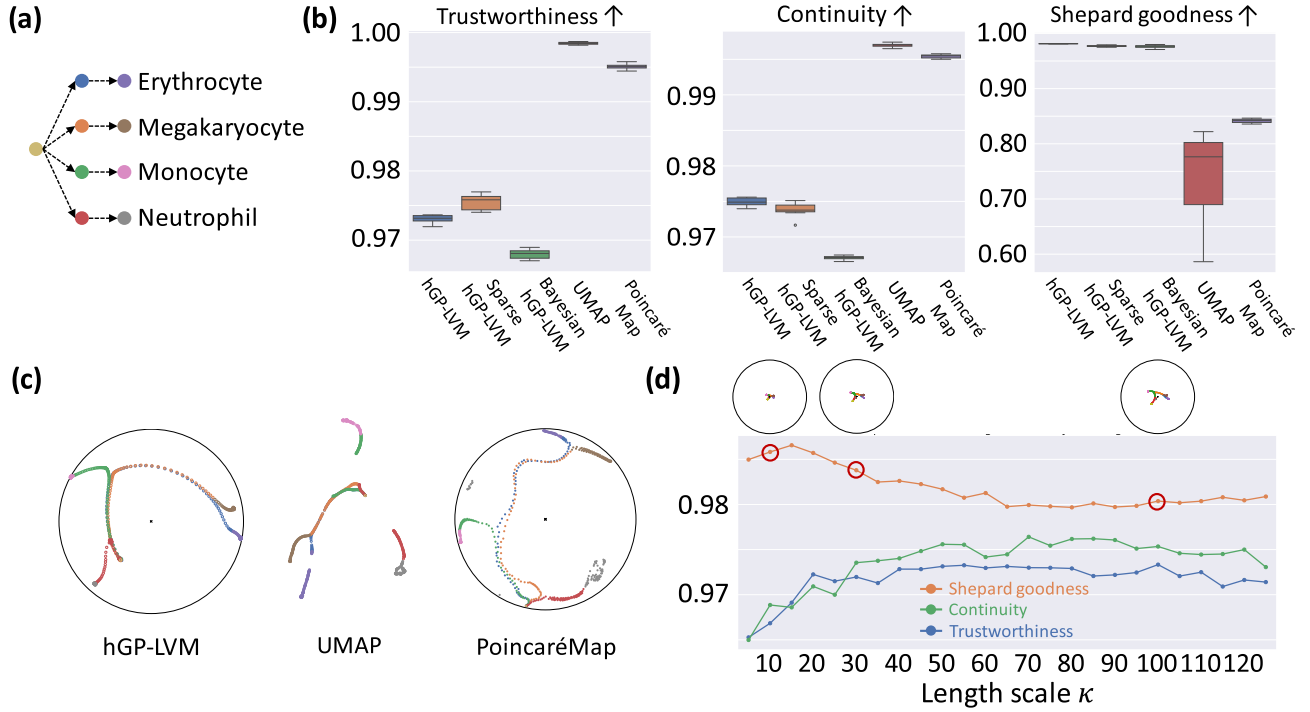


Figure A.2: **Experimental results on the synthetic myeloid progenitors dataset.** (a) Hierarchical relation and color code of visualization. (b) Error bar plot of trustworthiness (left), continuity (center), and Shepard goodness (right). (c) Scatter plot of two-dimensional embeddings of hGP-LVM, UMAP, and PoincaréMap. We zoomed in on latent variables and showed the original latent space in the upper left corner. (d) Quality metric scores of hGP-LVM with different length scales κ . (e) Comparison of reconstruction error of sparse hGP-LVM and sparse GP-LVM.

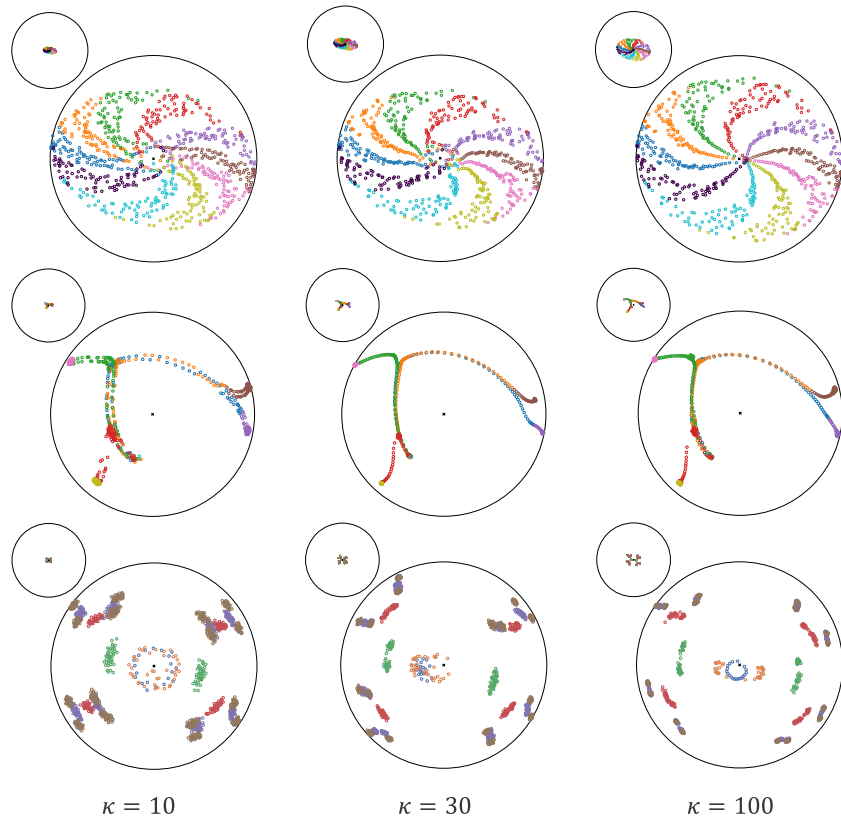


Figure A.3: **Embedding comparison of hGP-LVM with different length scales on synthetic datasets, Spiral (top), synthetic myeloid progenitors (middle), and SBT (bottom)).** We zoomed in on the latent variables.